Phase Feedforward Damping Control Method for Virtual Synchronous Generators

Li, Mingxuan; Yu, Peng; Hu, Weihao; Wang, Yue; Shu, Sirui; Zhang, Zhenyuan; Blaabjerg, Frede

Published in:
I E E E Transactions on Power Electronics

DOI (link to publication from Publisher):
10.1109/TPEL.2022.3150950

Publication date:
2022

Document Version
Accepted author manuscript, peer reviewed version

Phase Feedforward Damping Control Method for Virtual Synchronous Generators

Mingxuan Li, *Member, IEEE*, Peng Yu, Weihao Hu, *Senior Member, IEEE*, Yue Wang, *Member, IEEE*, Sirui Shu, Zhenyuan Zhang, *Senior Member, IEEE*, and Frede Blaabjerg, *Fellow, IEEE*

***Abstract*—Damping control plays an important role in suppressing the oscillation modes of virtual synchronous generators (VSGs). The most widely used damping control method through a frequency deviation feedback path is confronted with multiple challenging inherent contradictions among the different control objectives, resulting in seriously degraded control performance of VSGs. To resolve these contradictions fundamentally, this paper proposes a novel phase feedforward damping (PFD) control method for VSG from the perspective of restructuring the damping controller. It replaces the traditional frequency deviation feedback path with a novel damping controller utilizing a phase feedforward path. Then, considering the grid-connected and islanding operation modes, respectively, a detailed comparative study of the traditional damping-based VSG (Tra-VSG) and the PFD-based VSG (PFD-VSG) is conducted. Both the theoretical and experimental results demonstrate convincingly that the proposed PFD control method can reconcile the different control objects of VSG, and thus, compared with Tra-VSG, PFD-VSG exhibits vastly superior response performance of the active power and the frequency in both grid-connected and islanding operation modes.**

***Index Terms*—Damping control, response speed, oscillation suppression, frequency response, virtual synchronous generators (VSGs), voltage-source converters (VSCs).**

I. Introduction

With the development of distributed generation, the proportion of power electronic converters in the power systems is increasing very fast, thereby inducing the current trend towards converter-dominated power systems [1]-[3]. To cope with the frequency stability problems brought by the growing converters with low inertia and weak damping in the power systems, the virtual synchronous generator (VSG) control strategy has been proposed as an effective and promising solution to equip the grid-connected converters with the same functions and external characteristics as synchronous generators (SGs), e.g. providing inertia, damping, and primary frequency and voltage regulation services, etc., so that the converter-interfaced distributed generation units can be more compatible with the existing power grids, and thus can achieve a large-scale connection with the power systems easily [4]-[6].

Due to the introduction of virtual inertia, a VSG usually behaves as a typical second-order dynamic system and thereby needs to add proper damping to suppress the oscillation modes. The most straightforward way is to mimic the damping windings of SGs, together with the swing equation [6]-[8]. Unfortunately, due to the lack of magnetic coupling mechanism of SGs, VSGs have to depend on a phase-locked loop (PLL) to detect the grid frequency to produce the damping power, which contradicts the fundamental aims of VSGs and also incurs potential instability risks [9], [10]. Hence, a PLL-free damping control method has become the most widely used way to supply the damping effect by using the nominal frequency instead of the grid frequency in the PLL-based method [11]. Nevertheless, this approach has multiple challenging contradictions, which will degrade the control performance of VSGs seriously in various aspects.

a) There is a contradiction between the dynamic response indices of the active power, viz. the response speed and the overshoot suppression ability. This is an inherent problem of a second-order system, which the traditional PLL-free damping-based VSG (Tra-VSG) belongs to.

b) There is a contradiction between the goals of droop control and damping control. As it is well known, the droop control and the damping control in VSG are deployed for different purposes. However, the droop coefficient and the damping factor in Tra-VSG are equivalent to one identical parameter, resulting in a virtual impossibility of achieving the control goals of droop and damping simultaneously. Moreover, the power sharing performance among the VSGs will also be subjected to the impacts of the unwanted interaction between the droop and damping control.

c) There is a contradiction between the goals of accelerating the active power response and suppressing the frequency fluctuations. In power systems, active power is commonly expected to respond rapidly for reaching power balance fast, whereas it is preferable to exhibit a slow frequency dynamic response to restrain the fluctuations [12]. However, when tuning the parameters in the traditional PLL-free damping controller, the response speed of active power and that of frequency always change in the same trend, viz. becoming

Manuscript received October 1, 2021; revised January 9, 2022; accepted January 31, 2022. This work was supported by the National Natural Science Foundation of China (No. 51777159). (*Corresponding author: Weihao Hu.*)

M. Li, W. Hu and Z. Zhang are with the School of Mechanical and Electrical Engineering, University of Electronic Science and Technology of China, Chengdu 611731, China (email: limx@uestc.edu.cn; whu@uestc.edu.cn; zhangzhenyuan@uestc.edu.cn).

P. Yu, Y. Wang and S. Shu are with the School of Electrical Engineering, Xi'an Jiaotong University, Xi'an 710049, China (email: tinyfish0203@stu.xjtu.edu.cn; davidwangyue@mail.xjtu.edu.cn; ssr5dd@stu.xjtu.edu.cn).

F. Blaabjerg is with the Department of Energy Technology, Aalborg Unviersity, Aalborg 9220, Denmark (e-mail: fbl@et.aau.dk).

faster or slower at the same time.

Recently, numerous enhanced damping methods have been reported successively to improve the dynamic response of the frequency and/or the active power, including self-adapting parameter based, additional poles and zeros placement based, additional correction control loop based, virtual impedance based, state feedback based, Fuzzy control based, artificial intelligence (AI) based methods, etc. Therein, the self-adapting parameter based methods can obtain better dynamic responses of the active power and/or the frequency by regulating adaptively the parameters in VSG, e.g. the virtual inertia [13], [14], the damping factor [15], or the two parameters at the same time [16]-[20], etc. However, these methods are based on the traditional damping control structure, and therefore still fail to resolve the inherent contradictions mentioned above. Meanwhile, the nonlinearity of these methods complicates the design of the system. Moreover, the assessment of the stability and the seamless operation between the grid-connected and islanded modes still need further investigations. The additional poles and zeros placement based methods can also improve the damping control and optimize the dynamic response greatly by adding extra poles and/or zeros properly [9], [21], [22], but these methods usually need to utilize the derivate parts that are sensitive to noise, thereby being prone to incur instability. The additional correction control loop based methods insert one or more auxiliary control loops into the basic VSG controller to damp the power oscillations and adjust the dynamic response [23]-[25], which are at the cost of design complexity and risk of instability due to the introduction of the derivative parts. The virtual impedance based method takes full advantage of the damping effect of the output impedance to supplement the system damping and thus help the VSG to stabilize itself [26], [27]. Nevertheless, this group of methods still cannot settle the conflicts among the different control goals. Moreover, the damping effect provided by the impedance is always inadequate, and the auxiliary impedance will aggravate the power coupling, which impacts adversely on the system's performance and stability. The state feedback method is also used to develop a damping controller of VSG. Combined with a proper pole placement, this type of method demonstrates a strong dynamic response performance [28], [29]. However, these methods increase the design complexity dramatically, and the control performance heavily relies on the accuracy of the state observer or estimator. Moreover, fuzzy control [30], [31], and AI control [32], [34], have been applied to the VSG control strategy as well lately to improve the frequency stability, enhance the inertia response, and suppress the power oscillations. Despite the manifest superiority, this type of non-analytical method fails to reveal the internal mechanism. In addition, the design rules of the fuzzy controller must fully depend on the experience of the designer. The AI-based methods need to be based on long-time self-learning, and their complicated algorithms are difficult to be implemented by the present mainstream digital signal processors.

As a whole, the existing literature has not presented an effective damping control method to reconcile the diverse control objectives in VSG fundamentally. Motivated by this, this paper proposes a simple yet highly effective damping control method for VSG by utilizing a phase feedforward path instead of the traditional frequency deviation feedback path. In comparison to existing literature, the main contributions made in this paper and their significance are summarized as follows. First, the proposed idea breaks the limitation of mimicking SG and builds a novel mechanism of producing damping power. Accordingly, it resolves the inherent control contradictions in VSG radically and avoids the trade-off of the multiple control objectives, thereby simplifying the controller design and improving the VSG performance greatly. Second, the proposed damping control approach is simple, linear, based on fixed control parameters, with no need for derivate parts, and thus can be easily implemented in engineering. Practically, it can markedly enhance the response performance of the active power and the output frequency of VSG simultaneously in both the grid-connected and islanding operation modes by tuning only one parameter, i.e. the damping factor. Third, based on an in-depth analytical study, great insights into the internal mechanism of the multiple contradictions among the different control objectives in VSG are also given in this article.

The rest of the paper is organized as follows. In Section II, two groups of the most typical damping control strategies, viz. the traditional PLL-based and PLL-free damping control strategies are introduced and analyzed, and then the novel PFD control scheme is presented. Further, detailed comparative analyses between Tra-VSG and PFD-VSG under two scenarios, grid-connected and islanding operation modes, are conducted in Sections III and IV. Then, the grid-connected and islanding experiments are shown to verify the theoretical analysis in Section V. Finally, Section VI makes the concluding remarks.

II. Different Damping Control Methods of VSGs

Fig. 1 (a) and (b) depict a complete and a simplified diagram of a grid-connected VSG system, respectively. Therein, P_{ref} and Q_{ref} are the active and reactive power references, P and Q are the output active and reactive power, u_{abc} and i_{abc} are the output voltages and output currents of VSG, E and θ are the amplitude (in RMS) and phase of the output voltage of VSG, L_f and C_f are the filter inductance and capacitor, C is the DC-side capacitor, X is the equivalent connection impedance between the VSG and the grid, δ is the power angle, viz. the phase difference between the VSG and the grid, and U is RMS value of the grid voltage.

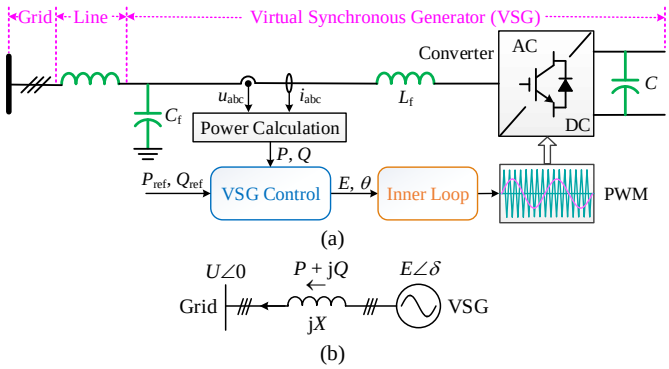

Fig. 1. Grid-connected VSG system. (a) Diagram of circuit and control system; (b) Simplified diagram.

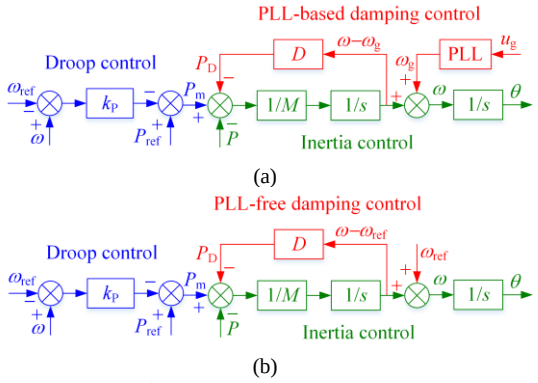

(a)

(b)

Fig. 2. Block diagram of a VSG using traditional damping control. (a) PLL-based damping control; (b) PLL-free damping control (Tra-VSG).

The VSG control achieves the regulation of the output active power and reactive power by controlling the phase and amplitude of the output voltage, respectively. The inner loop can employ the frequently used cascaded voltage and current controller to obtain better control flexibility and performance [35].

Next, the different damping control methods, together with the VSG control, will be explained in detail.

A. Traditional Damping Control Methods of VSGs

1) Traditional PLL-based damping control method

A complete VSG control strategy, including virtual inertia control, droop control, and damping control, can be expressed mathematically as

$$M\frac{\mathrm{d}(\omega-\omega_{\mathrm{g}})}{\mathrm{d}t}=P_{\mathrm{m}}-P-P_{\mathrm{D}} \tag{1}$$

where $M = J\omega_{\mathrm{ref}}$, J is the virtual inertia, ω_{ref} is the nominal angular frequency, ω is the output angular frequency, ω_{g} is the grid angular frequency, P is the output active power, P_{D} is the damping power used for suppressing the oscillations, P_{m} is the virtual mechanical power produced by the droop control, and it can be written by

$$P_{\mathrm{m}}=P_{\mathrm{ref}}-k_{\mathrm{P}}\left(\omega-\omega_{\mathrm{ref}}\right) \tag{2}$$

where P_{ref} is the active power reference, and k_{P} is the P-ω droop coefficient.

The block diagram of a VSG using a PLL-based damping control is depicted in Fig. 2 (a). Therein, the PLL-based damping controller mimics the mechanism of damping windings in SG, namely producing an additional damping power based on the deviation between the output frequency and the grid frequency, which can be expressed by

$$P_{\mathrm{D}}=D(\omega-\omega_{\mathrm{g}}) \tag{3}$$

where D is the damping factor. The fundamental principle of the PLL-based damping control is attempting to pull the active power back to the equilibrium point by adding P_{D} to P_{m} or subtracting P_{D} from P_{m} properly according to the sign of $\omega-\omega_{\mathrm{g}}$.

However, different from the SG, due to the lack of a physical magnetic field coupling mechanism like SG, VSG has to rely on a PLL to detect the frequency deviation, viz. $\omega-\omega_{\mathrm{g}}$, to produce the damping power. However, the dependency of PLL on the grid voltage contradicts the basic objective of VSG, viz. having voltage source characteristics with independently-controlled output voltage amplitude and frequency and thereby possessing a grid-forming ability. Consequently, the PLL-based method is not suitable for the current trend of converter-dominated power systems. Besides, the PLL-based method is affected by the performance of the PLL and even incurs instability issues or failures when the grid voltage fluctuates, becomes distorted, or the grid is weakly connected, etc.

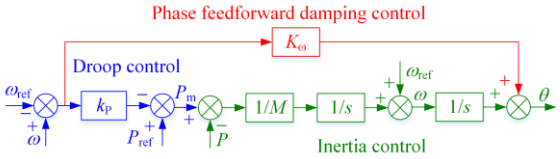

Fig. 3. Block diagram of a VSG using proposed PFD control (PFD-VSG).

2) Traditional PLL-free damping control

Accordingly, the PLL-based damping control method has been replaced by the PLL-free method. Nowadays, the PLL-free method has become the most widely-used method, whose block diagram can be drawn as Fig. 2 (b). The main difference between the PLL-based and the PLL-free damping methods is that the latter uses the nominal frequency instead of the grid frequency to produce the damping power, thereby expressing the damping power as

$$P_{\mathrm{D}}=D(\omega-\omega_{\mathrm{ref}}) \tag{4}$$

It can be seen that the damping power described by (4) has the same mathematical expression as the droop control expressed by (2). In other words, the droop coefficient and the damping factor play the same role in the control loop and can be regarded as one identical parameter. However, the function of the droop coefficient is to provide the frequency-supporting service required by the power systems and to match with the other converters to share the power proportionally, whereas the function of the damping factor is to suppress the oscillation modes of the control system. Practically, the optimal ranges of the droop coefficient and the damping factor usually do not overlap. As a result, the traditional PLL-free damping control method can hardly achieve the damping and droop control goals at the same time. This is one of the major deficiencies of the PLL-free damping control method, and other deficiencies will be analyzed in detail in Sections III and IV.

B. Proposed Phase Feedforward Damping (PFD) Control Method

To address the deficiencies of the traditional PLL-free damping control method, this paper proposes a novel damping control method by utilizing a phase feedforward path instead of the traditional frequency deviation feedback path. The block diagram of a VSG employing the proposed phase feedforward damping method, called PFD-VSG for short, is depicted in Fig. 3. Therein, K_{ω} is the gain of the phase feedforward path. Similar to D in Tra-VSG, enlarging K_{ω} can add the damping to the closed-loop system, which will be analyzed in detail hereinafter. For this reason, K_{ω} can also be called the damping factor of PFD-VSG.

Next, Sections III and IV will conduct a detailed comparative analysis between PFD-VSG and Tra-VSG in two typical applications, viz. the grid-connected operation mode and the islanding operation mode.

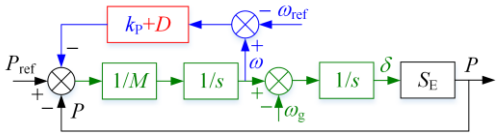

Fig. 4. Block diagram of the closed-loop model of a grid-connected Tra-VSG.

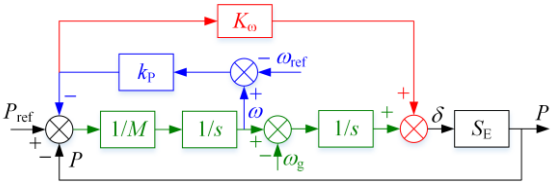

Fig. 5. Block diagram of the closed-loop model of a grid-connected PFD-VSG.

TABLE I
MAIN PARAMETERS FOR SINGLE-UNIT GRID-CONNECTED SYSTEM

Parameter	Description	Value
U_n	Nominal/basic voltage	220 V (RMS)
P_n	Nominal/basic power	10 kW
U	Grid voltage (phase-ground)	220 V (RMS)
U_{dc}	DC-side voltage	750 V
f_s	Switching frequency	10 kHz
C	DC-side capacitor	850 μF
L_f	Filter inductance	0.4 mH
C_f	Filter capacitor	30 μF
ω_{ref}	Nominal angular frequency	100π rad/s (50 Hz)
ω_g	Grid angular frequency	100π rad/s (50 Hz)
J	Moment of inertia	1 kg·m^2
k_P	Droop coefficient	5000/π W/(rad/s)
X	Connection impedance	0.22 pu

III. COMPARATIVE ANALYSIS OF TRA-VSG AND PFD-VSG IN GRID-CONNECTED MODE

The grid-connected operation mode is analyzed firstly, and the system configuration is as shown in Fig. 1. The main parameters used for the analyses and the later tests are listed in TABLE I.

Accordingly, the closed-loop block diagrams of the grid-connected Tra-VSG and PFD-VSG systems can be drawn in Figs. 4–5, respectively. Therein, s is the Laplace operator, S_E is the synchronizing power coefficient, satisfying $S_E = 3EU\cos\delta/X \approx 3EU/X$.

The output active power and frequency of the grid-connected VSG are the most concerned output variables, and their dynamic response characteristics can be used to evaluate the performance of the control strategies and the parameters inside. Based on the closed-loop models of Tra-VSG and PFD-VSG, the dynamic characteristics of the active power and frequency are comparatively analyzed as follows. Subsequently, the system stability is also compared.

A. Dynamic Characteristics of Output Active Power

1) $\Delta P/\Delta P_{ref}$

According to the closed-loop model of the grid-connected Tra-VSG shown in Fig. 4, the active power closed-loop transfer function of the Tra-VSG can be expressed as

$$G_{\text{PPref\_Tra}}(s) = \frac{\Delta P}{\Delta P_{\text{ref}}} = \frac{S_E}{Ms^2 + (k_P + D)s + S_E} \tag{5}$$

where the subscript "Tra" or the later "PFD" are used to state that the variable or function is specifically used for the Tra-VSG or PFD-VSG.

It can be found that $G_{\text{PPref\_Tra}}(s)$ represents a typical second-order system, whose characteristic function is

$$Ms^2 + (k_P + D)s + S_E = 0 \tag{6}$$

where the undamped natural angle frequency ω_n and the damping ratio ζ can be obtained as

$$\omega_{n\_Tra} = \sqrt{\frac{S_E}{M}}, \qquad \zeta_{Tra} = \frac{k_P + D}{2\sqrt{MS_E}} \tag{7}$$

Likewise, the active power closed-loop transfer function of the PFD-VSG can be obtained from Fig. 5 as

$$G_{\text{PPref\_PFD}}(s) = \frac{\Delta P}{\Delta P_{\text{ref}}} = \frac{K_\omega k_P S_E s + S_E}{Ms^2 + (k_P + K_\omega k_P S_E)s + S_E} \tag{8}$$

Then, the characteristic function of the PFD-VSG is

$$Ms^2 + (k_P + K_\omega k_P S_E)s + S_E = 0 \tag{9}$$

Further, calculating the corresponding undamped natural angle frequency and the damping ratio yields, respectively,

$$\omega_{n\_PFD} = \sqrt{\frac{S_E}{M}}, \qquad \zeta_{PFD} = \frac{k_P + K_\omega k_P S_E}{2\sqrt{MS_E}} \tag{10}$$

By comparing (7) and (10), it can be seen that they have the same natural frequency, and the role of damping factor D in the damping ratio is replaced with $k_P K_\omega S_E$. Hence, once k_P and S_E are set, K_ω plays the same role in the PFD-VSG as D in the damping control of Tra-VSG. Therefore, K_ω can be regarded as the damping factor of PFD-VSG. Regulating D in Tra-VSG or K_ω in PFD-VSG can make an adjustment of the damping ratio.

Moreover, compared with $G_{\text{PPref\_Tra}}(s)$, $G_{\text{PPref\_PFD}}(s)$ has an extra derivative term in the numerator, which brings a zero to the system. This derivative term can predict the occurrence of an overshoot ahead of time and produce a proper counteraction timely to hinder the tendency towards a too large overshoot. Therefore, it can help in accelerating the dynamic response of the active power. It should be emphasized that despite benefiting from the derivative term in $G_{\text{PPref\_PFD}}(s)$, the actual control scheme does not include a derivative part, and hence avoids a potential instability risk caused by a derivative control.

Fig. 6 presents the bode diagrams of $\Delta P/\Delta P_{ref}$ of Tra-VSG and PFD-VSG with the different damping ratios, respectively, which illustrate the active power dynamic characteristics following an active power reference disturbance.

As explained before, $G_{\text{PPref\_Tra}}(s)$ of Tra-VSG is a typical second-order system. Therefore, as shown in Fig. 6 (a), if the damping ratio is too small, e.g. $\zeta = 0.4$, the bode diagram will exhibit a resonance peak before the cutting frequency, which indicates that an oscillation at the resonance frequency will appear. By enlarging the damping ratio, the resonance peak will be suppressed gradually, thereby inhibiting the overshoots of the step response. However, on the other hand, the increase of the damping ratio also narrows the bandwidth, implying a slower dynamic response. As a consequence, the tuning of the damping ratio for Tra-VSG has to trade off the overshoot suppression ability against the response speed. Generally, it is advisable to select the damping ratio in the interval of [0.707, 1].

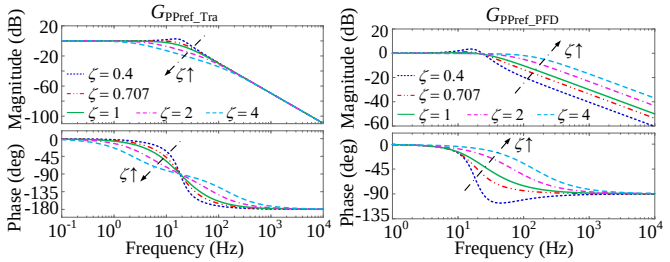

Fig. 6. Bode diagrams of active power responses under a disturbance of active power reference ($\Delta P/\Delta P_{\text{ref}}$) for a grid-connected VSG system. (a) Tra-VSG; (b) PFD-VSG.

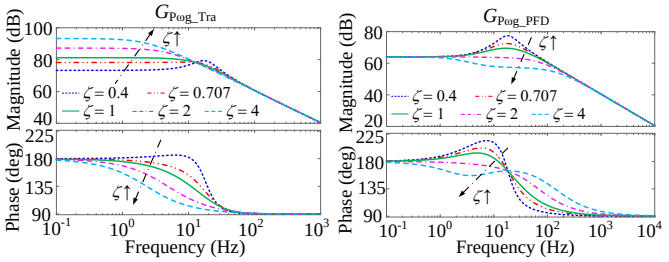

Fig. 7. Bode diagrams of active power responses under a disturbance of grid frequency ($\Delta P/\Delta\omega_{\text{g}}$) for a grid-connected VSG system. (a) Tra-VSG; (b) PFD-VSG.

By contrast, the zero that exists in $G_{\text{PPref\_PFD}}(s)$ of PFD-VSG has a significant impact on the dynamic response of the active power. First, as shown in Fig. 6 (b), the increase of the damping ratio also restrains the resonance peak and weakens the oscillations, which is similar to Tra-VSG. Nevertheless, opposite to Tra-VSG, augmenting the damping ratio of PFD-VSG will increase the bandwidth, which suggests that a larger damping ratio can bring a faster dynamic response. To sum up, enlarging the damping ratio of PFD-VSG can make both the overshoot suppression ability and the dynamic response speed of the active power move towards the optimal performance indices at the same time. Hence, for PFD-VSG, a larger damping ratio ζ, viz. a larger damping factor K_{ω}, is desirable.

In conclusion, according to the above theoretical analysis, we can discover the first important advantage of PFD-VSG over Tra-VSG: PFD-VSG resolves the contradiction between the response speed and overshoot suppression ability of the active power, and thus it can obtain a fast active power response with no overshoots.

2) $\Delta P/\Delta\omega_{\text{g}}$

The closed-loop transfer functions of Tra-VSG and PFD-VSG from the grid frequency disturbance to the output active power can be expressed as

$$G_{\text{P}\omega\text{g\_Tra}}(s) = \frac{\Delta P}{\Delta\omega_{\text{g}}} = -\frac{S_{\text{E}}\left(Ms + k_{\text{P}} + D\right)}{Ms^2 + (k_{\text{P}} + D)s + S_{\text{E}}} \tag{11}$$

$$G_{\text{P}\omega\text{g\_PFD}}(s) = \frac{\Delta P}{\Delta\omega_{\text{g}}} = -\frac{S_{\text{E}}\left(Ms + k_{\text{P}}\right)}{Ms^2 + (k_{\text{P}} + K_{\omega}k_{\text{P}}S_{\text{E}})s + S_{\text{E}}} \tag{12}$$

It can be observed from (11) and (12) that both of them are typical second-order systems with a zero. When $D = K_{\omega}k_{\text{P}}S_{\text{E}}$, they have the same characteristic functions, and the main differences between them are the steady-state gains and the locations of the zeros. The bode diagrams of $\Delta P/\Delta\omega_{\text{g}}$ of Tra-VSG and PFD-VSG with varying damping ratios can be plotted in Fig. 7 (a) and (b), respectively.

First, both the resonance peaks of Tra-VSG and PFD-VSG can be suppressed with the increase of the damping ratio. Second, as the damping ratio grows, the steady-state gain of Tra-VSG rises continuously, meaning that the output active power will go up. Essentially, this is the result of the unwanted impacts of the traditional PLL-free damping controller on the droop control. Conversely, no matter how the damping ratio varies, the steady-state gain of PFD-VSG always maintains a constant of 64 dB, matching with the pre-set droop coefficient k_{P} = 10 kW/Hz exactly.

Mathematically, the active power dynamic response of Tra-VSG and PFD-VSG can be expressed as

$$P_{\text{Tra}} = G_{\text{PPref\_Tra}}(s)P_{\text{ref}} - G_{\text{P}\omega\text{g\_Tra}}(s)(\omega_{\text{ref}} - \omega_{\text{g}}) \tag{13}$$

$$P_{\text{PFD}} = G_{\text{PPref\_PFD}}(s)P_{\text{ref}} - G_{\text{P}\omega\text{g\_PFD}}(s)\left(\omega_{\text{ref}} - \omega_{\text{g}}\right) \tag{14}$$

Calculating the limits of (13) and (14) yields

$$\begin{aligned} P_{0\_\text{Tra}} &= \lim_{s\to 0} G_{\text{PPref\_Tra}}(s)P_{\text{ref}} - \lim_{s\to 0} G_{\text{P}\omega\text{g\_Tra}}(s)\left(\omega_{\text{ref}} - \omega_{\text{g}}\right) \\ &= P_{\text{ref}} + \left(k_{\text{P}} + D\right)\left(\omega_{\text{ref}} - \omega_{\text{g}}\right) \end{aligned} \tag{15}$$

$$\begin{aligned} P_{0\_\text{PFD}} &= \lim_{s\to 0} G_{\text{PPref\_PFD}}(s)P_{\text{ref}} - \lim_{s\to 0} G_{\text{P}\omega\text{g\_PFD}}(s)\left(\omega_{\text{ref}} - \omega_{\text{g}}\right) \\ &= P_{\text{ref}} + k_{\text{P}}\left(\omega_{\text{ref}} - \omega_{\text{g}}\right) \end{aligned} \tag{16}$$

By comparing (15) and (16), it can be seen that, due to the effect of the damping control, the equivalent droop coefficient of Tra-VSG changes from k_{P} to k_{P}+D, whereas the droop coefficient of PFD-VSG is always k_{P} and free from the influence of the damping control. Hence, for PFD-VSG, increasing the damping factor only enhances the ability to suppress dynamic oscillations but does not impact the static droop control. This is the second advantage of PFD-VSG: PFD-VSG eliminates the interactions between the droop control and the damping control.

B. Dynamic Characteristics of Output Frequency

1) $\Delta\omega/\Delta P_{\text{ref}}$

The closed-loop transfer functions of Tra-VSG and PFD-VSG from the active power reference to the output angular frequency can be derived as

$$G_{\omega\text{Pref\_Tra}}(s) = \frac{\Delta\omega}{\Delta P_{\text{ref}}} = \frac{s}{Ms^2 + (k_{\text{P}} + D)s + S_{\text{E}}} \tag{17}$$

$$G_{\omega\text{Pref\_PFD}}(s) = \frac{\Delta\omega}{\Delta P_{\text{ref}}} = \frac{s}{Ms^2 + \left(k_{\text{P}} + K_{\omega}k_{\text{P}}S_{\text{E}}\right)s + S_{\text{E}}} \tag{18}$$

When $D = K_{\omega}k_{\text{P}}S_{\text{E}}$, Tra-VSG and PFD-VSG have the same frequency dynamic response under a disturbance of active power reference. Likewise, the bode diagrams of $G_{\omega\text{Pref\_Tra}}(s)$ and $G_{\omega\text{Pref\_PFD}}(s)$ for different damping ratios are plotted in Fig. 8. It can be seen that both the bode diagrams show resonance peaks around the damped natural frequency, indicating that the dynamic response waveforms of output frequency in the time domain will have oscillations or overshoots during a step. With the increase of the damping ratios, the resonance peaks of the two methods both decline but cannot be eliminated thoroughly, showing that the overshoots of the time-domain waveforms cannot be suppressed completely.

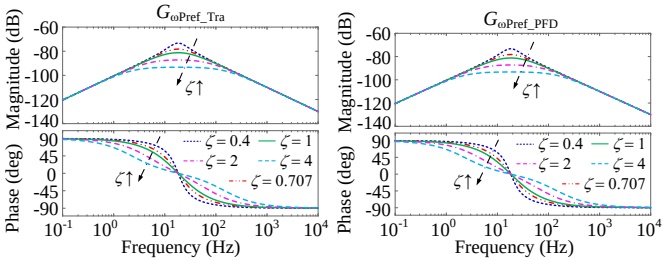

Fig. 8. Bode diagrams of output frequency responses under a disturbance of active power reference ($\Delta\omega/\Delta P_{ref}$) for a grid-connected VSG system. (a) Tra-VSG; (b) PFD-VSG.

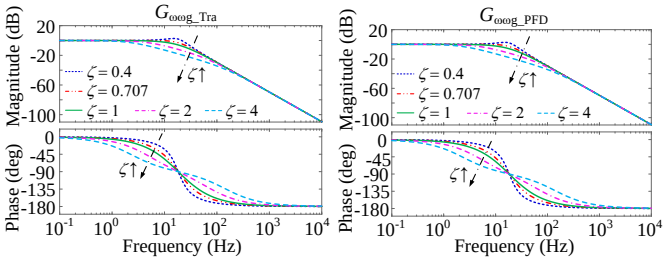

Fig. 9. Bode diagrams of output frequency responses under a disturbance of grid frequency ($\Delta\omega/\Delta\omega_g$) for a grid-connected VSG system. (a) Tra-VSG; (b) PFD-VSG.

2) $\Delta\omega/\Delta\omega_g$

Then, the closed-loop transfer functions of Tra-VSG and PFD-VSG from the grid angular frequency to the output angular frequency can also be obtained as

$$G_{\omega\omega g\_Tra}(s) = \frac{\Delta\omega}{\Delta\omega_g} = \frac{S_E}{Ms^2 + (k_P + D)s + S_E} \tag{19}$$

$$G_{\omega\omega g\_PFD}(s) = \frac{\Delta\omega}{\Delta\omega_g} = \frac{S_E}{Ms^2 + (k_P + K_\omega k_P S_E)s + S_E} \tag{20}$$

Similarly, when $D = K_\omega k_P S_E$, the frequency dynamic responses of Tra-VSG and PFD-VSG following a grid frequency disturbance can be described by an identical second-order system. The corresponding bode diagrams for different damping ratios are shown in Fig. 9. In normal cases, the damping ratio is commonly chosen between 0.707 and 1 to balance the overshoot suppression performance and the response time. However, the output frequency response of a grid-connected VSG is a very special case, which aims at restraining the fluctuations and slowing down the changing rate. Therefore, both Tra-VSG and PFD-VSG prefer larger damping ratios to achieve more desirable output frequency responses.

By summarizing the impacts of the damping controllers of Tra-VSG and PFD-VSG on the active power and frequency responses, it can be concluded that, compared with Tra-VSG, PFD-VSG can reconcile the need for fast active power response and the desire for slow output frequency response. Specifically, for Tra-VSG, when the damping ratio is adjusted, the response speed of active power and that of frequency will change in the same trend, and in other words, the active power and frequency responses will become either faster or slower at the same time. However, the active power expects a faster response, while a slower output frequency response is desirable. Consequently, the tuning of the damping ratio of Tra-VSG needs to balance the dynamic responses of the active power and the frequency, while for PFD-VSG, adding the damping ratio can accelerate the active power response and slow down the output frequency response simultaneously. Hence, both the optimal performances of the active power and the frequency can easily be achieved. This is the third advantage of PFD-VSG over Tra-VSG: PFD-VSG resolves the contradiction between the objectives of the active power and the frequency control.

As a whole, the above theoretical analyses demonstrate the proposed PFD-VSG can resolve the inherent contradictions in Tra-VSG, indicating that the PFD-VSG has better control performance of the active power and the frequency. Moreover, because PFD removes the coupling between the droop control and the damping control, the pivotal parameters in PFD-VSG,

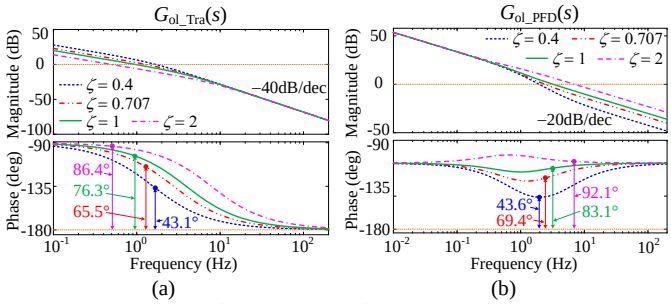

Fig. 10. Bode diagrams of open-loop transfer functions of grid-connected VSG when ζ = 0.4, 0.707, 1, 2. (a) Tra-VSG; (b) PFD-VSG.

including virtual inertia J, droop coefficient k_P, and damping factor K_ω, can be designed easily and flexibly. First, the virtual inertia J is selected considering the grid requirements and the dynamic characteristics of the DC-side generation source. Then, the droop coefficient k_P is chosen to meet the requirements of the primary frequency control. Third, when J and k_P are set, the damping factor K_ω can be calculated according to the optimal damping ratio ζ. Generally, it is suggested that ζ is larger than 1, and ζ around 2 is desirable in the above case.

C. Stability Analysis of Grid-connected System

Notice that when choosing the same damping ratio, the Tra-VSG and PFD-VSG have identical characteristic equations, viz. (6) and (9). Therefore, the locations of the poles do not change following the insertion of the feedforward damping path. Namely, the PFD does not influence the absolute stability of the gird-connected VSG. Nevertheless, due to the introduction of zero, the relative stability will be impacted, which can be quantified by the stability margins.

The open-loop transfer functions of the grid-connected Tra-VSG and PFD-VSG system can be obtained as

$$G_{ol\_Tra}(s) = \frac{S_E}{Ms^2 + (k_P + D)s} \tag{21}$$

$$G_{ol\_PFD}(s) = \frac{K_\omega k_P S_E s + S_E}{Ms^2 + k_P s} \tag{22}$$

Accordingly, the bode diagrams of (21) and (22) are plotted in Fig. 10. It can be seen that when the damping ratio ζ is set as 0.4, 0.707, 1, and 2, respectively, the phase margins (PMs) of Tra-VSG are 43.1°, 65.5°, 76.3°, and 86.4°, whereas the PMs of PFD-VSG are 43.6°, 69.4°, 83.1°, and 92.1°. It can be found that the PM of PFD-VSG is enlarged due to the effect of the additional zero, and thereby the PFD-VSG exhibits superior stability to the Tra-VSG. Besides, enlarging the damping ratio is beneficial to stability and both the Tra-VSG and PFD-VSG

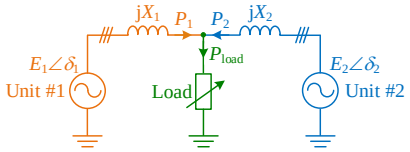

Fig. 11. Diagram of a two-unit system with a common load.

TABLE II
DIFFERENTIATED PARAMETERS FOR THE TWO-UNIT SYSTEM

Description		Unit #1		Unit #2
Basic/Nominal power	P_{n1}	10 kW	P_{n2}	20 kW
Moment of inertia	J_1	1 kg·m^2	J_2	4 kg·m^2
Droop coefficient	k_{P1}	5/π kW/(rad/s)	k_{P2}	10/π kW/(rad/s)
Connection impedance	X_1	0.2 pu	X_2	0.4 pu
Damping ratio	ζ_1	Case I: [0.4, 2] Case II: 1	ζ_2	Case I: $\zeta_2=\zeta_1$ Case II: [0.4, 2]

will have desirable PMs when the damping ratio is set reasonably, e.g. $\zeta \geq 0.707$.

On the other hand, the declining slope in the high-frequency range of the PFD-VSG becomes –20dB/dec while the Tra-VSG is –40dB/dec, implying that PFD-VSG has a reduced rejection ability of high-frequency interference. Fortunately, the inputs of the feedforward damping path of PFD-VSG are the angular frequency reference and the output of the inertia controller. The former always keeps constant during the operation, and the latter always changes very slowly because of the big virtual inertia. Thereby, the reduction in the rejection ability of high-frequency signals will not exert a great influence on the anti-interference performance of PFD-VSG.

IV. COMPARATIVE ANALYSIS OF TRA-VSG AND PFD-VSG IN ISLANDING MODE

In this section, the performances of Tra-VSG and PFD-VSG in the islanding operation mode are analyzed comparatively. Here, a parallel two-unit system connected to a common load is taken as a paradigm of the islanding operation for the later analysis, which is depicted in Fig. 11. Similar conclusions can also be drawn according to a larger multiple-unit system. The differentiated parameters of the units are listed in TABLE II, and the other parameters of the units are still set uniformly according to TABLE I.

A. Modeling of a Two-unit System with a Common Load

The block diagram of the equivalent closed-loop model of the parallel Tra-VSG and PFD-VSG system can be drawn as Fig. 12 (a) and (b), respectively [36]. Then, the allocated active power for the ith unit can be calculated as

$$\Delta P_i = \frac{S_{E1}S_{E2}}{S_{E1}+S_{E2}}\left(\Delta\theta_i - \Delta\theta_j\right) + \frac{S_{Ei}}{S_{E1}+S_{E2}}\Delta P_{load} \quad (23)$$

where i and j indicate the serial number of the units, here $i = 1$, $j = 2$ or $i = 2$, $j = 1$, ΔP_{load} is the disturbance of the common load, and S_{Ei} is the synchronizing power coefficient of the ith unit, satisfying

$$S_{Ei} = \frac{3E_iU_i}{X_i}\cos\delta_i,\ i=1,2. \quad (24)$$

The equivalent open-loop transfer functions from the allocated active power to the output phase and the output angular frequency of the ith Tra-VSG or PFD-VSG, which are

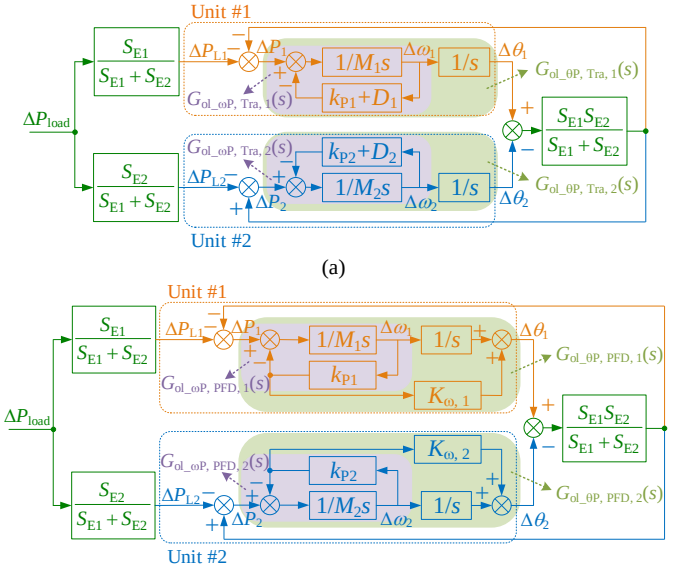

Fig. 12. Block diagram of the equivalent closed-loop model of the parallel two-unit system with a common load. (a) Tra-VSG; (b) PFD-VSG.

highlighted by purple and green backgrounds in Fig. 12 (a) and (b), respectively, can be described mathematically by

$$G_{ol\_\theta P,\,Tra,\,i} = \frac{\Delta\theta_{Tra,\,i}}{\Delta P_{Tra,\,i}} = \frac{1}{M_is^2 + \left(k_{Pi}+D_i\right)s},\ i=1,2. \quad (25)$$

$$G_{ol\_\theta P,\,PFD,\,i} = \frac{\Delta\theta_{PFD,\,i}}{\Delta P_{PFD,\,i}} = \frac{1+K_{\omega i}k_{Pi}s}{M_is^2 + k_{Pi}s},\ i=1,2. \quad (26)$$

$$G_{ol\_\omega P,\,Tra,\,i} = \frac{\Delta\omega_{Tra,\,i}}{\Delta P_{Tra,\,i}} = \frac{1}{M_is + k_{Pi} + D_i},\ i=1,2. \quad (27)$$

$$G_{ol\_\omega P,\,PFD,\,i} = \frac{\Delta\omega_{PFD,\,i}}{\Delta P_{PFD,\,i}} = \frac{1}{M_is + k_{Pi}},\ i=1,2. \quad (28)$$

where the subscripts "Tra" or "PFD" are used to state that the variable or function is specifically used for the Tra-VSG or PFD-VSG, similarly hereinafter.

Then, the closed-loop active power transfer functions of the ith Tra-VSG and PFD-VSG can be derived as

$$G_{P\_Tra,\,i}(s) = \frac{\Delta P_{Tra,\,i}}{\Delta P_{load}} = \frac{1}{1+\dfrac{G_{ol\_\theta P,\,Tra,\,i}(s) - 1/S_{Ei}}{G_{ol\_\theta P,\,Tra,\,j}(s) - 1/S_{Ej}}} \quad (29)$$

$$G_{P\_PFD,\,i}(s) = \frac{\Delta P_{PFD,\,i}}{\Delta P_{load}} = \frac{1}{1+\dfrac{G_{ol\_\theta P,\,PFD,\,i}(s) - 1/S_{Ei}}{G_{ol\_\theta P,\,PFD,\,j}(s) - 1/S_{Ej}}} \quad (30)$$

where $i = 1$, $j = 2$ or $i = 2$, $j = 1$.

Further, the closed-loop frequency transfer functions of the ith Tra-VSG and PFD-VSG can be written as

$$G_{\omega\_Tra,\,i}(s) = \frac{\Delta\omega_{Tra,\,i}}{\Delta P_{load}} = \frac{G_{ol\_\omega P,\,Tra,\,i}(s)}{1+\dfrac{G_{ol\_\theta P,\,Tra,\,i}(s) - 1/S_{Ei}}{G_{ol\_\theta P,\,Tra,\,j}(s) - 1/S_{Ej}}} \quad (31)$$

$$G_{\omega\_PFD,\,i}(s) = \frac{\Delta\omega_{PFD,\,i}}{\Delta P_{load}} = \frac{G_{ol\_\omega P,\,PFD,\,i}(s)}{1+\dfrac{G_{ol\_\theta P,\,PFD,\,i}(s) - 1/S_{Ei}}{G_{ol\_\theta P,\,PFD,\,j}(s) - 1/S_{Ej}}} \quad (32)$$

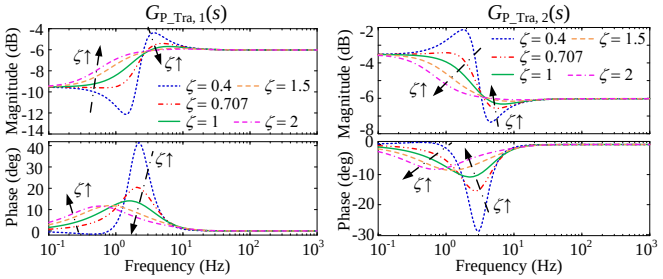

Fig. 13. Bode diagrams of active power responses of Tra-VSGs under Case I ($\zeta_1 = \zeta_2$). (a) Unit #1; (b) Unit #2.

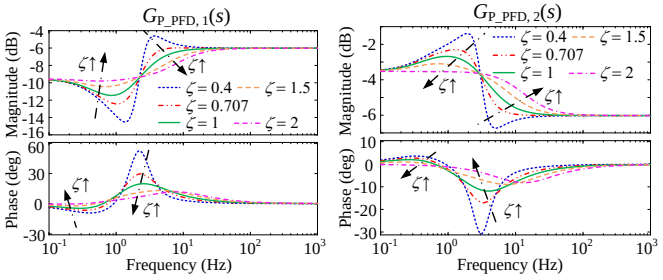

Fig. 14. Bode diagrams of active power responses of PFD-VSGs under Case I ($\zeta_1 = \zeta_2$). (a) Unit #1; (b) Unit #2.

where $i = 1$, $j = 2$ or $i = 2$, $j = 1$.

By using the closed-loop transfer functions, the dynamic response characteristics of the active powers and the output angular frequencies can be analyzed further.

B. *Case I: $\zeta_1 = \zeta_2$*

The case in which the units have the same damping ratio is firstly considered.

1) Dynamic response of output active power

Comparing (29) and (30), the active power transfer functions of Tra-VSG and PFD-VSG have the same forms but different poles and zeros. The corresponding bode diagrams are plotted in Figs. 13–14, respectively.

First, it can be seen that, for both the Tra-VSGs and PFD-VSGs, when the system is undamped, the bode diagram of unit #1 has a concave resonance peak while unit #2 has a convex one. It implies that the step response of unit #1 has a descending overshoot while that of unit #2 has an ascending overshoot. Then, as the damping ratios increase, the resonance peaks of Tra-VSGs and PFD-VSGs are both reduced, which indicates smaller oscillations and overshoots. Differently, the resonance peak of Tra-VSG disappears when $\zeta \geq 1$, whereas the resonance peak of PFD-VSG is eliminated until $\zeta \geq 2$. Second, adding the damping ratios narrows the bandwidths of both the Tra-VSGs and thus the Tra-VSGs will exhibit slower dynamic responses. Conversely, both the PFD-VSGs will get larger bandwidths with the increase of damping ratios, thereby having faster dynamic responses. In other words, the Tra-VSGs in the islanding operation mode also face the same contradiction as the grid-connected mode, viz. the contradiction between obtaining faster dynamic response and enhancing the overshoot suppress ability. By contrast, the PFD-VSGs in islanding mode can resolve this contradiction as well and it can achieve better dynamic performance than the Tra-VSGs. Third, because the per-unit values of the parameters of the two units in (29) and (30) are well-matched, for Tra-VSG and PFD-VSG, the ratios

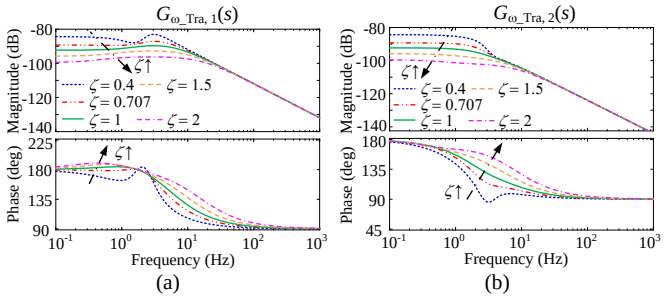

Fig. 15. Bode diagrams of output frequency responses of Tra-VSGs under Case I ($\zeta_1 = \zeta_2$). (a) Unit #1; (b) Unit #2.

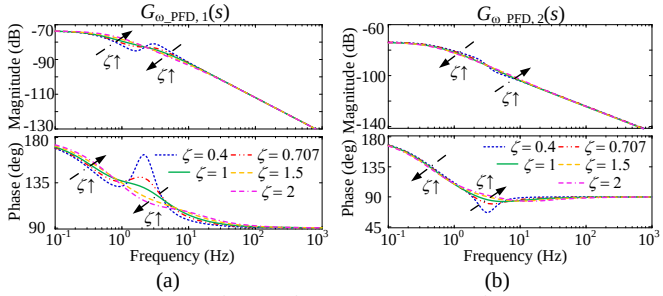

Fig. 16. Bode diagrams of output frequency responses of PFD-VSGs under Case I ($\zeta_1 = \zeta_2$). (a) Unit #1; (b) Unit #2.

of the steady-state gains of unit #1 and unit #2 are equal to k_{P1}/k_{P2}, and do not change following the damping ratios. It indicates that the active power can be shared as planned for both the Tra-VSG and PFD-VSG system under Case I.

2) Dynamic response of output frequency

Figs. 15–16 show the bode diagrams of the output angular frequency responses of the Tra-VSGs and the PFD-VSGs, respectively, according to (31) and (32).

With the increase of the damping ratios, the gains of both the Tra-VSGs in the low-frequency range decrease gradually, while the low-frequency gains of the PFD-VSGs remain unchanged. Calculating the limits of $G_{\omega\_Tra}(s)$ and $G_{\omega\_PFD}(s)$ at zero, respectively, yields

$$\lim_{s\to 0} G_{\omega\_Tra,i}(s) = \frac{1}{k_{P1} + D_1 + k_{P2} + D_2},\ i = 1, 2. \tag{33}$$

$$\lim_{s\to 0} G_{\omega\_PFD,i}(s) = \frac{1}{k_{P1} + k_{P2}},\ i = 1, 2. \tag{34}$$

It can be seen that the equivalent droop coefficient of the parallel Tra-VSG system declines as the damping factors grow. Consequently, the ω-P characteristics will become excessively flat, resulting in a risk of turning a small error in the control system, e.g. the sampling error, into an extremely large error of the output active power. On the contrary, the proposed phase feedforward damping control method can avoid this negative impact. No matter how the damping factors of the PFD-VSGs vary, the steady-state gains of $G_{\omega\_PFD,1}(s)$ and $G_{\omega\_PFD,2}(s)$ are always dominated by the pre-set droop coefficients, so that the system can always maintain the pre-designed optimal droop characteristics.

In terms of dynamic responses, unit #1 of the parallel Tra-VSG system always has a small and gentle resonance peak at a few Hz even when $\zeta \geq 1$, which implies that an overshoot will occur after a load disturbance, whereas both the PFD-VSGs have no resonance peaks and thereby no overshoots. Moreover, all the magnitudes in the high-frequency range of the Tra-VSGs

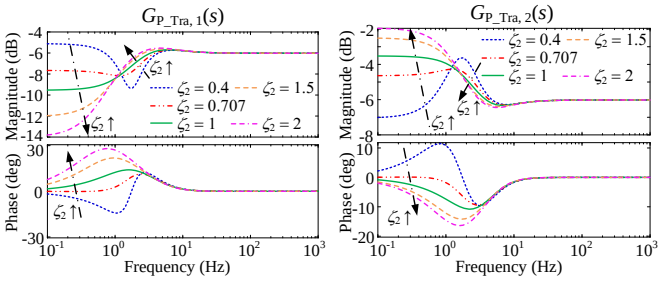

Fig. 17. Bode diagrams of active power responses of Tra-VSGs under Case II ($\zeta_1 \neq \zeta_2$). (a) Unit #1; (b) Unit #2.

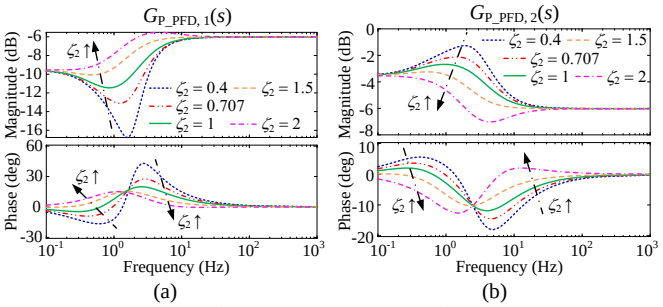

Fig. 18. Bode diagrams of active power responses of PFD-VSGs under Case II ($\zeta_1 \neq \zeta_2$). (a) Unit #1; (b) Unit #2.

and PFD-VSGs drop at a slope of –20dB/dec, and thereby both the Tra-VSG and PFD-VSG have a decent rejection ability of high-frequency interference in this islanding case.

C. *Case II: $\zeta_1 \neq \zeta_2$*

This section will further discuss the case of the units with different damping ratios. Specifically, keep ζ_1 equal to 1 and change ζ_2 in the range of [0.4, 2], and observe the responses of the output active power and frequency of the two units.

1) Dynamic response of output active power

Calculating the limits of $G_{P\_Tra}(s)$ and $G_{P\_PFD}(s)$, respectively, yields

$$\lim_{s\to 0} G_{P\_Tra,i}(s) = \frac{k_{Pi} + D_i}{k_{P1} + D_1 + k_{P2} + D_2},\ i = 1, 2. \tag{35}$$

$$\lim_{s\to 0} G_{P\_PFD,i}(s) = \frac{k_{Pi}}{k_{P1} + k_{P2}},\ i = 1, 2. \tag{36}$$

Therefore, the power sharing between the units can be obtained as

$$\frac{\Delta P_{Tra,1}}{\Delta P_{Tra,2}} = \frac{\lim\limits_{s\to 0} G_{P\_Tra,1}(s)}{\lim\limits_{s\to 0} G_{P\_Tra,2}(s)} = \frac{k_{P1} + D_1}{k_{P2} + D_2} \tag{37}$$

$$\frac{\Delta P_{PFD,1}}{\Delta P_{PFD,2}} = \frac{\lim\limits_{s\to 0} G_{P\_PFD,1}(s)}{\lim\limits_{s\to 0} G_{P\_PFD,2}(s)} = \frac{k_{P1}}{k_{P2}} \tag{38}$$

According to (37), the active power sharing proportion between the Tra-VSGs depends on both the droop coefficients and damping factors. When k_{P1}, k_{P2}, and D_1 are set, the variation of D_2 will have a remarkable impact on the active power sharing. When ζ_2 increases, viz. D_2 increases, $\Delta P_1/\Delta P_2$ will get smaller, deviating from the planned sharing ratio. It can be proved by the bode diagrams of the Tra-VSGs as shown in Fig. 17. With the enlargement of ζ_2, the steady-state gain of unit #1 declines continuously while the steady-state gain of unit #2 goes up accordingly.

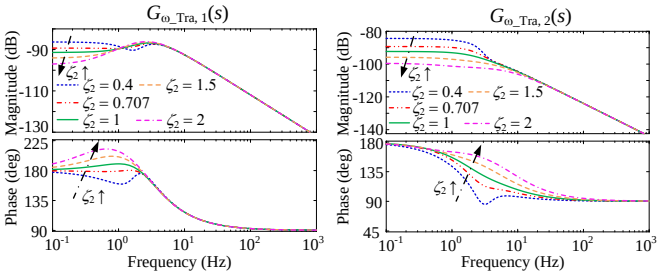

Fig. 19. Bode diagrams of output frequency responses of Tra-VSGs under Case II ($\zeta_1 \neq \zeta_2$). (a) Unit #1; (b) Unit #2.

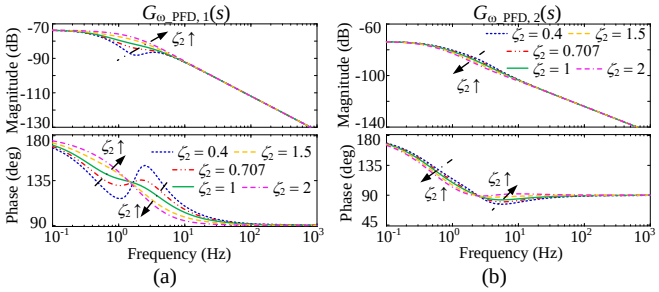

Fig. 20. Bode diagrams of output frequency responses of PFD-VSGs under Case II ($\zeta_1 \neq \zeta_2$). (a) Unit #1; (b) Unit #2.

By contrast, for the parallel PFD-VSG system, the steady-state gains of the units always remain unchanged, as shown in Fig. 18. It can be seen from (38) that no matter how ζ_2 varies, the active power sharing between PFD-VSGs always remains to be the planned ratio of the droop coefficients, viz. k_{P1}/k_{P2}, which is independent of the damping factors. Generally, the droop coefficients are set according to the power ratings of the units. In a conclusion, the PFD-VSG eliminates the negative impact of the damping control on the droop control, and hence the PFD-VSG is more advantageous to accurate power sharing than the Tra-VSG.

Concerning the transient characteristics, the increase of ζ_2 can suppress the resonance peaks of the two units. However, when ζ_2 is too large, the reverse resonance peaks appear instead, indicating the occurrence of reverse overshoots in the time-domain waveforms. The reason for this phenomenon is that the difference between the damping ratios of the two units is too great. Accordingly, it is satisfying to choose ζ_2 larger slightly than ζ_1 for parallel PFD-VSG systems. As for Fig. 17, $\zeta_2 = 1.5$ is a good choice.

2) Dynamic response of output frequency

The bode diagrams of the output frequency responses for parallel Tra-VSG system and parallel PFD-VSG system are shown in Figs. 19–20, respectively.

For a parallel Tra-VSG system, both the steady-state gains of the two units descend following the growth of ζ_2. On the contrary, for a parallel PFD-VSG system, the steady-state gains of the two units keep unchanged. Therefore, the Tra-VSGs increase the risk of producing a large control error due to a too flat ω-P characteristic, whereas the PFD-VSGs can always maintain the optimal droop characteristics, regardless of the tuning of the damping control, which is the same as in Case I.

In terms of the dynamic response, due to the difference between the damping ratios of the Tra-VSGs, a growing convex resonance will arise in the bode diagram of the first Tra-VSG as ζ_2 increases to a certain extent, e.g. $\zeta_2 \geq 1$ in Fig. 19 (a), while

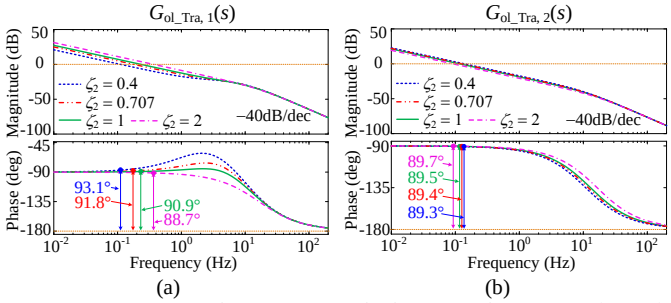

Fig. 21. Bode diagrams of open-loop transfer functions of Tra-VSGs (ζ_1 = 1, ζ_2 = 0.4, 0.707, 1, 2). (a) Unit #1; (b) Unit #2.

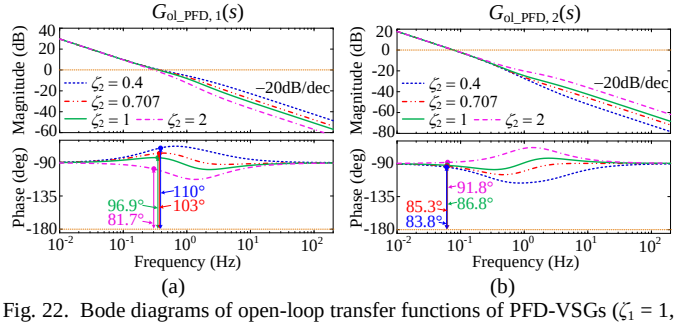

Fig. 22. Bode diagrams of open-loop transfer functions of PFD-VSGs (ζ_1 = 1, ζ_2 = 0.4, 0.707, 1, 2). (a) Unit #1; (b) Unit #2.

the second Tra-VSG does not produce any resonance peaks. In contrast, for the parallel PFD-VSG system, both the PFD-VSGs do not exhibit any resonance peaks with the rise of ζ_2. Therefore, the first Tra-VSG will have an overshoot during a load change while both the PFD-VSGs will not. Besides, they have the same ability to reject the high-frequency interference due to the same declining speed (−20dB/dec) in the high-frequency range.

D. Stability Analysis of Islanding System

According to Fig. 12, the open-loop transfer functions of the Tra-VSGs and PFD-VSGs can be obtained as

$$G_{\text{ol\_Tra},i} = \frac{K \cdot G_{\text{ol\_}\theta\text{P, Tra},i}}{1 + K \cdot G_{\text{ol\_}\theta\text{P, Tra},i}}, \quad i = 1, 2. \tag{39}$$

$$G_{\text{ol\_PFD},i} = \frac{K \cdot G_{\text{ol\_}\theta\text{P, PFD},i}}{1 + K \cdot G_{\text{ol\_}\theta\text{P, PFD},i}}, \quad i = 1, 2. \tag{40}$$

where $K = S_{E1}S_{E2}/(S_{E1}+S_{E2})$.

Then, keep ζ_1 equal to 1 and change ζ_2 in the range of [0.4, 2]. The bode diagrams of the open-loop transfer functions of the Tra-VSGs and PFD-VSGs can be plotted further in Figs. 21–22. It can be seen that under different damping ratios, both the Tra-VSG and PFD-VSG have sufficiently large PMs (around 90°). Therefore, it can be concluded that both the islanding Tra-VSG and PFD-VSG systems exhibit very fine stability. Besides, it should be emphasized that, although the declining slope in the high-frequency range of the open-loop bode plots of the PFD-VSG becomes −20dB/dec which seems smaller than −40dB/dec of the Tra-VSG, by comparing the closed-loop responses of the two output variables, viz. the output active power and angular frequency as shown in Figs. 17–20, the Tra-VSG and PFD-VSG systems have the same closed-loop declining slope in the high-frequency range, implying that the islanding Tra-VSG and PFD-VSG systems have a similar anti-interference ability of the responses of the active power and output frequency.

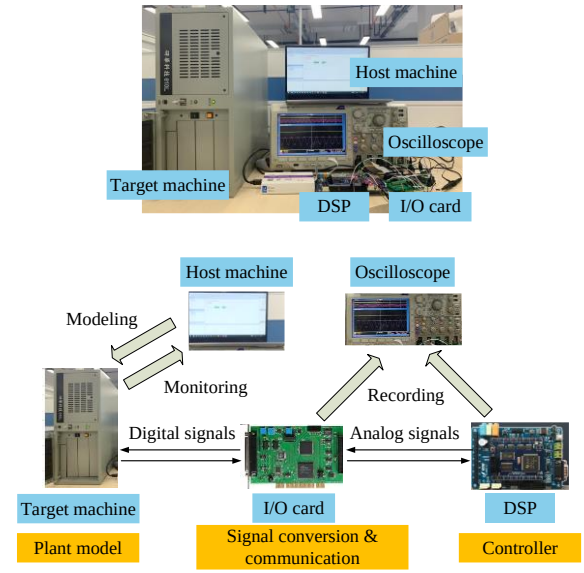

Fig. 23. Photograph and setup of the HIL platform.

V. Experimental Verification

A hardware-in-loop (HIL) platform is built to verify the aforesaid theoretical conclusions, whose photograph and setup are shown in Fig. 23. Therein, the tested circuits operate in real time with a step size of 8 μs in the target machine, and the control algorithms of the Tra-VSGs or the PFD-VSGs run in DSPs TMS320F28335 with clock cycles of 1/150 μs. The conversion and communication of the signals between the target machine and DSP peripheral circuit are realized by multifunction I/O cards Humusoft MF624. The waveforms and data are monitored and recorded by an oscilloscope in real time.

The experiments are conducted in two scenarios, viz. a single-unit grid-connected system, and a parallel two-unit system with a common load, to verify the performance of the proposed damping control method in grid-connected mode and islanding mode, respectively. The tested systems and the experimental parameters are the same as those used for the foregoing theoretical analysis, as shown in Fig. 1 (a) and Fig. 11 and listed in TABLEs I and II, respectively.

A. Single-Unit Grid-connected System

This section is to test the grid-connected performance by using a single-unit system connecting to the grid.

1) $\Delta P_e/\Delta P_{\text{ref}}$

The active power waveforms of Tra-VSG and PFD-VSG in the case that P_{ref} steps up from 0 to 5 kW at t_0 are shown in Fig. 24 (a) and (b), respectively. Therein, the colorful solid lines are the experimental waveforms, and the black thin dotted lines are the results of the theoretical models built in Section III, which are the same as the later experimental waveforms. It can be observed that the theoretical results coincide very closely with the experimental results.

According to Fig. 24 (a), in terms of Tra-VSG, with the increase of the damping ratio ζ, the overshoot is suppressed gradually. When $\zeta \geq 1$, the overshoot disappears completely. On the other hand, a greater damping ratio also makes the settling time to become longer, indicating a slower response.

It can be further observed from Fig. 24 (b) that, for PFD-VSG,

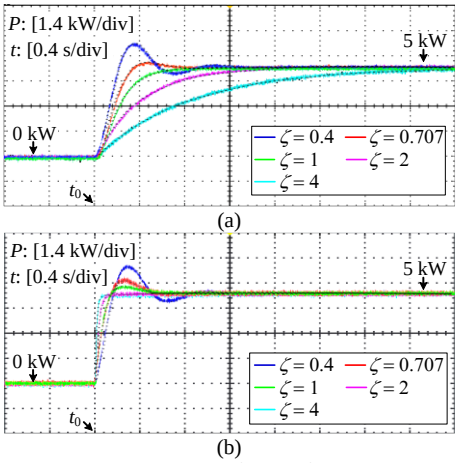

Fig. 24. Active power response waveforms of a grid-connected VSG with different damping ratios when the active power reference steps from 0 to 5 kW at t_0. (a) Tra-VSG; (b) PFD-VSG.

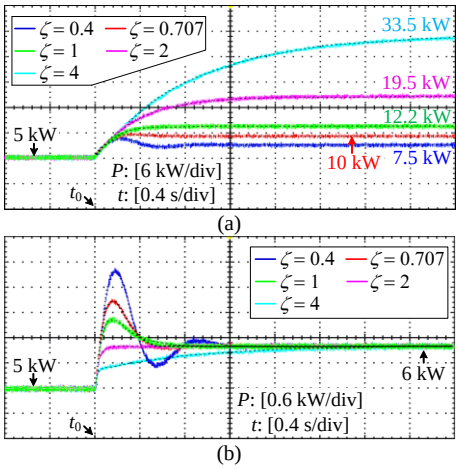

Fig. 25. Active power response waveforms of a grid-connected VSG with different damping ratios when the grid frequency steps from 50 Hz to 49.9 Hz at t_0. (a) Tra-VSG; (b) PFD-VSG.

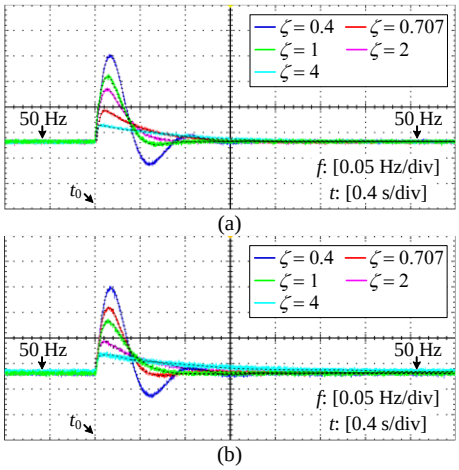

Fig. 26. Response waveforms of the output frequency of a grid-connected VSG with different damping ratios when the active power reference steps from 0 to 5 kW at t_0. (a) Tra-VSG; (b) PFD-VSG.

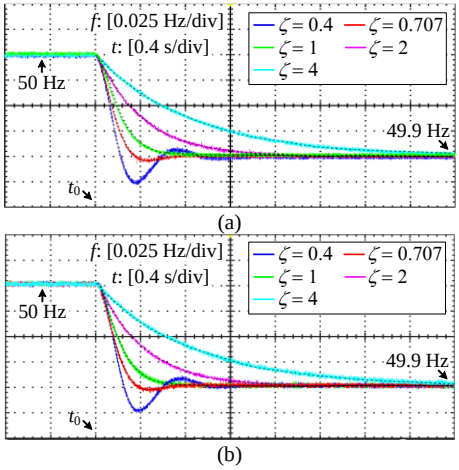

Fig. 27. Response waveforms of the output frequency of a grid-connected VSG with different damping ratios when the grid frequency steps from 50 Hz to 49.9 Hz at t_0. (a) Tra-VSG; (b) PFD-VSG.

the overshoot can also be restrained effectively by increasing the damping ratio ζ. But, due to the effect of the zero, there still exists a little overshoot when $\zeta = 1$. The overshoot disappears finally until $\zeta \geq 2$. Concerning the response time, PFD-VSG has an opposite rule compared with Tra-VSG. Namely, adding the damping ratio of the PFD-VSG reduces the settling time of the active power, thereby obtaining a faster dynamic response. Accordingly, an optimal K_ω can be found to achieve a no-overshoot and fast response at the same time.

The above experimental results demonstrate the superiority of the PFD-VSG over Tra-VSG in addressing the contradiction between a stronger overshoot suppression ability and a faster response of the output active power, which is consistent with the previous theoretical analysis.

2) $\Delta P_e/\Delta\omega_g$

Fig. 25 (a) and (b) show the active power waveforms of Tra-VSG and PFD-VSG following a grid frequency disturbance. To begin with, the VSG operates stably with P_{ref} = 5 kW. At t_0, the grid frequency steps down from 50 Hz to 49.9 Hz.

Concerning Tra-VSG, according to Fig. 25 (a), although the oscillation is inhibited with the increase of the damping ratio, yet the steady-state value of active power after the disturbance becomes undesirably large. Actually, according to the pre-set droop coefficient k_P, viz. 10 kW/Hz, the steady-state value of active power should stay at 6 kW. However, due to the unwanted effect of the damping control, except for the deviation caused by the droop control, an extra error is also produced. Taking the case of $\zeta = 1$ as an example, viz. D = 62 kW/Hz accordingly, the extra error even reaches 6.2 kW (P = 12.2 kW). As a consequence, it would incur severely uneven power sharing problems and possibly an overload fault.

Unlike Tra-VSG, the output active power of PFD-VSG with different K_ω after the grid frequency disturbance always maintains at the planned value of 6 kW. Therefore, it validates the advantage of PFD-VSG over Tra-VSG in avoiding the adverse impacts of the damping control on the droop control.

Besides, for PFD-VSG, the settling time of active power will decrease at first and rise afterwards as the damping ratio increases. Accordingly, there is an optimal value of K_ω to obtain the best dynamic performance ($\zeta = 2$ is superb in this test).

3) $\Delta\omega/\Delta P_{ref}$

Fig. 26 shows the output frequency response waveforms of the Tra-VSG and PFD-VSG following an active power reference step from 0 to 5 kW at t_0, which look the same because

their transfer functions can be regarded as one when their damping factors are matched. Hence, the Tra-VSG and PFD-VSG can be discussed together.

It can be seen that the growing damping ratios can make the overshoots smaller, the rise times shorter, and the settling times shorter at first and longer afterwards. Meanwhile, as the damping ratios rise, the overshoots can be reduced continuously but cannot be eliminated, which agrees with the theoretical analysis based on Fig. 8. Practically, very large damping ratios can make the overshoots so small that the maximum deviations are not too far from the final steady-state values. In this case, although the settling times increase, the variation rates of the frequencies also decline, which is more favorable to the frequency stability. From this perspective, larger damping ratios, namely a bigger D in Tra-VSG or a bigger K_ω in PFD-VSG, are preferable.

4) $\Delta\omega/\Delta\omega_g$

Fig. 27 shows the output frequency response waveforms of Tra-VSG and PFD-VSG following a grid frequency step from 50 Hz to 49.9 Hz at t_0. Likewise, the Tra-VSG and the PFD-VSG have similar transfer functions of the $\Delta\omega/\Delta\omega_g$ and can be discussed together. As it can be seen, enlarging the damping ratios can suppress and even eliminate the overshoots, and also make the output frequency responses slower. Therefore, it can be concluded that larger damping ratios are also more suitable for both Tra-VSG and PFD-VSG concerning the dynamic response of $\Delta\omega/\Delta\omega_g$.

5) Comparison of overall performance

Further, to test the overall performance of Tra-VSG and PFD-VSG with the optimized parameters in the grid-connected application, a comparative experiment is conducted for Tra-VSG with $\zeta = 0.707$, Tra-VSG with $\zeta = 1$, and PFD-VSG with $\zeta = 2$. The active power and frequency waveforms are shown in Fig. 28. At first, the VSG works normally with no output active power. At t_0, the active power reference steps from 0 to 10 kW, and after 1.6 s, the grid frequency steps from 50 Hz to 50.1 Hz.

According to Fig. 28 (a), the active power waveform of Tra-VSG with $\zeta = 0.707$ exhibits a small overshoot following the P_{ref} step because of the insufficient damping. Then, the active power falls from 10 kW to 5.5 kW after the grid frequency step and a very mall downward overshoot also appears. Actually, according to the pre-set droop coefficient, viz. 10 kW/Hz, the planned output active power should be 9 kW. The deviation of 3.5 kW is caused by the undesirable effect of the damping control on the droop control. For eliminating the overshoot, $\zeta \geq 1$ should be set, e.g. the purple waveforms. It can be observed that, due to the rise of the damping ratio, although the overshoots disappear, the active power response of Tra-VSG with $\zeta = 1$ becomes slower. Moreover, when the grid frequency steps to 50.1 Hz, the deviation of active power is enlarged further. The steady-state value declines to 2.8 kW with an error of 6.2 kW. By contrast, in terms of the proposed PFD-VSG in this article, the active power has the fastest response (0.3 s shorter than Tra-VSG with $\zeta = 1$) and does not exhibit any overshoots. Above all, the damping control of PFD-VSG has no impact on droop control. The output active power always

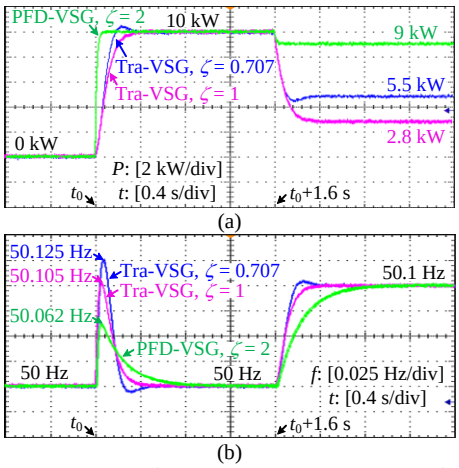

Fig. 28. Active power and frequency power response waveforms of grid-connected Tra-VSG and PFD-VSG when the active power reference steps from 0 to 10 kW at t_0 and then grid frequency steps from 50 Hz to 50.1 Hz at t_0 + 1.6s. (a) Active power; (b) Frequency.

remains to be the planned value of 9 kW with no error.

Further, to guarantee a fast enough response speed of active power, Tra-VSG cannot be chosen with a too large damping ratio. As a consequence, the overshoot of the output frequency of Tra-VSG cannot be suppressed adequately. As shown in Fig. 28 (b), the frequency overshoots are 50.125 Hz for $\zeta = 0.707$ and 50.105 Hz for $\zeta = 1$. However, PFD-VSG can obtain superior output frequency response at $\zeta = 2$, whose overshoot is only 50.062 Hz. Besides, the output frequency response of the PFD-VSG after a grid frequency step is slower than the Tra-VSGs, which demonstrates that PFD-VSG has a stronger ability to maintain frequency stability.

As a whole, the proposed PFD-VSG exhibits vastly superior performance than Tra-VSG in the responses of both the active power and the frequency.

B. Two-Unit System with a Common Load

This section will test the performance of Tra-VSG and PFD-VSG in islanding operation mode by using a parallel two-unit system connecting to a common load, where the units employ both Tra-VSG strategies or both PFD-VSG strategies. Two cases, viz. $\zeta_1 = \zeta_2$, and $\zeta_1 \neq \zeta_2$, are considered, respectively.

1) Case I: $\zeta_1 = \zeta_2$

In Case I, the two units employ the same damping ratio, viz. $\zeta_1 = \zeta_2$. The load steps from 0 to 10 kW at t_0. The corresponding experimental waveforms of the active power and the frequency of Tra-VSGs and PFD-VSGs following a load step under different damping ratios are given in Figs. 29–30.

First, the active power responses are analyzed. For the parallel Tra-VSG system as shown in Fig. 29 (a), by increasing the damping ratio ζ, the oscillations and overshoots of the active power responses of both the Tra-VSGs are suppressed gradually. Until $\zeta \geq 1$, the overshoots are eliminated fully. However, the active power responses are also slowed down following the growth of ζ. By contrast, in terms of the PFD-VSGs, as shown in Fig. 29 (b), the enlargement of ζ can also restrain the overshoots of both units effectively. The overshoots disappear completely when $\zeta \geq 1.5$. Fortunately, unlike Tra-VSGs, the responses of the PFD-VSGs are accelerated with the

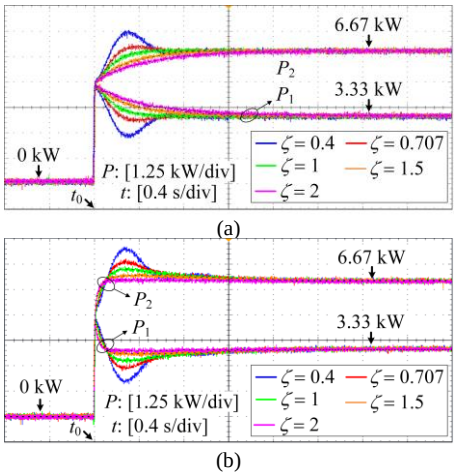

Fig. 29. Active power response waveforms of the two-unit system in Case I ($\zeta_1 = \zeta_2$) with the different damping ratios when the load steps from 0 to 10 kW at t_0. (a) Tra-VSGs; (b) PFD-VSGs.

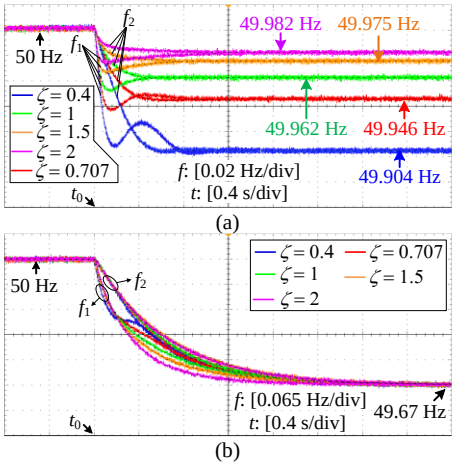

Fig. 30. Response waveforms of the output frequencies of the two-unit system in Case I ($\zeta_1 = \zeta_2$) with the different damping ratios when the load steps from 0 to 10 kW at t_0. (a) Tra-VSGs; (b) PFD-VSGs.

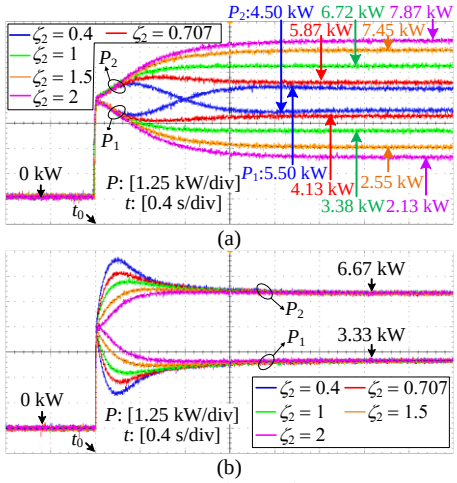

Fig. 31. Active power response waveforms of the two-unit system in Case II ($\zeta_1 \neq \zeta_2$) with $\zeta_1 = 1$ and a changing ζ_2 when the load steps from 0 to 10 kW at t_0. (a) Tra-VSGs; (b) PFD-VSGs.

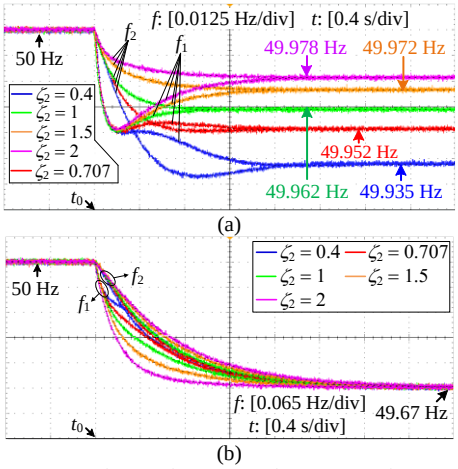

Fig. 32. Response waveforms of the output frequencies of the two-unit system in Case II ($\zeta_1 \neq \zeta_2$) with $\zeta_1 = 1$ and a changing ζ_2 when the load steps from 0 to 10 kW at t_0. (a) Tra-VSGs; (b) PFD-VSGs.

growth of ζ. This illustrates the superiority of PFD-VSG in optimizing the overshoot suppression ability and response speed of the active power simultaneously. Meanwhile, no matter the parallel Tra-VSG system or the parallel PFD-VSG system, when $\zeta_1 = \zeta_2$, the active power sharing proportion maintains always 1:2, viz. the ratio of the droop coefficients of the two units, as a result of the well-matched parameters.

Then, the responses of the output frequency are analyzed. The output frequency waveforms of the two units shown in Fig. 30 demonstrate that overshoots of the Tra-VSGs are reduced by adding the damping. However, the steady-state deviations of the frequencies of the Tra-VSGs after the disturbance are reduced because adding the damping factors also means augmenting the droop coefficients of the Tra-VSGs. Although a smaller frequency deviation is preferable, this also incurs an extremely flat ω-P characteristic, thereby raising the risk of turning tiny control deviations into very large output errors. On the contrary, the final steady-state frequencies of the parallel PFD-VSG system are always kept constant, which are only controlled by the pre-designed droop characteristics, avoiding the effects of the damping control. Further, considering the transient responses, both the parallel Tra-VSG and PFD-VSG systems exhibit a small rate of change of frequency, implying that they both realize desired inertia control. Besides, unit #1 of the parallel Tra-VSG system always exhibits an overshoot or oscillation even when $\zeta > 1$. On the contrary, both the PFD-VSGs do not have any overshoots or oscillations even when the damping ratio is very small, e.g. $\zeta = 0.4$ shown in Fig. 30 (b). The transient processes of the frequencies of PFD-VSGs are rather gentle. The above experimental phenomena coincide well with the theoretical conclusions.

2) Case II: $\zeta_1 \neq \zeta_2$

In case II, the damping ratio of unit #1 is designed to be 1, and the damping ratio of unit #2 varies among 0.4, 0.707, 1, 1.5, and 2. The active power and frequency waveforms of Tra-VSGs and PFD-VSGs are shown in Figs. 31–32, where the common load steps from 0 to 10 kW at t_0.

It can be seen from Fig. 31(a) that, except for the damping effects similar to Case I, the power sharing between the parallel Tra-VSGs also changes with the variation of ζ_2. With the rise of ζ_2, the output active power of unit #1 drops continuously from 5.50 kW ($\zeta_2 = 0.4$) to 2.13 kW ($\zeta_2 = 2$), and the active

TABLE III
ADVANTAGES OF PFD-VSG OVER TRA-VSG

Advantages \ Reasons	① PFD-VSG resolves the contradiction between response speed and overshoot suppression ability of active power.	② PFD-VSG resolves the contradiction between droop control and damping control.	③ PFD-VSG resolves the contradiction between the objectives of active power and frequency control.
Grid-Connected mode	-- PFD-VSG can optimize overshoot suppression ability and response speed of active power simultaneously, and thereby can obtain a faster active power response with no overshoots.	-- Damping control of PFD-VSG does not affect the steady-state output active power. -- PFD-VSG achieves both the goals of droop control and damping control.	-- PFD-VSG obtains desirable active power and output frequency responses simultaneously, i.e. fast active power response yet small frequency fluctuation.
Islanding mode	-- PFD-VSGs can obtain better dynamic characteristics of the output active power over Tra-VSGs.	-- PFD-VSGs always keep predesigned ω-P characteristics, regardless of the impact of damping control. -- PFD-VSG is more advantageous to accurate power sharing than Tra-VSG. -- PFD-VSGs avoid the excessively flat ω-P characteristics and prevent small errors in the control system from turning into large errors of output active power.	-- Under the preconditions of desired response of output frequency, dynamic performance of active power of PFD-VSG can also be improved further. -- PFD-VSGs have gentler transient processes of frequency without any overshoots and fluctuations.

power of unit #2 increases accordingly from 4.50 kW (ζ_2 = 0.4) to 7.87 kW (ζ_2 = 2). The corresponding power-sharing ratio P_1:P_2 changes from 1.22:1 to 0.27:1, which deviates from the pre-designed 1:2.

Unlike Tra-VSGs, as shown in Fig. 31(b), the power sharing between the PFD-VSGs can always remain 1:2 no matter how ζ_2 varies, which is only dominated by the pre-designed droop coefficients according to the power ratings of the two units. Therefore, it demonstrates the advantage of the PFD method in eliminating the poor impacts of the damping control on power sharing.

Moreover, it can be observed from Fig. 31 that, for the same damping ratios, the active powers of PFD-VSGs have a smaller settling time and thereby have a faster dynamic response speed than Tra-VSGs. On the other hand, reverse overshoots in parallel PFD-VSG system can be observed when ζ_2 is much larger than ζ_1, e.g. ζ_2 = 2, which agrees well with the theoretical analysis shown in Fig. 18.

In terms of the output frequency responses shown in Fig. 32, firstly for the parallel Tra-VSG system, the first overshoot of unit #1 after the disturbance does not change with the variation of ζ_2. When $\zeta_2 < \zeta_1$=1, unit #2 also has an overshoot, and a smaller ζ_2 means a longer settling time. When ζ_2 is added, the overshoot of unit #2 is suppressed gradually. Until $\zeta_2 \geq \zeta_1$=1, the overshoot of unit #2 is eliminated fully, and a larger ζ_2 means a slower dynamic response.

Then, considering the parallel PFD-VSG system, the steady-state values of the frequencies after the disturbances always maintain a fixed value of 49.67 Hz as designed by the droop control. Furthermore, the frequencies of both the units do not have any overshoots and can arrive at the final steady-state operating points gently, which indicates that the PFD control maintains the inertia characteristics of VSG pretty well.

The above experimental results verify the conclusions drawn by the previous theoretical analysis and demonstrate the superior performance of the PFD-VSG compared with the Tra-VSG. The primary reason for these superiorities is the PFD-VSG fundamentally resolves the three inherent contradictions among the different control objectives of Tra-VSG. Finally, TABLE III summarizes these advantages of the PFD-VSG and the corresponding primary reasons in both grid-connected and islanding operation modes.

VI. Conclusions

This paper proposes a simple but highly effective phase feedforward damping (PFD) control method for VSG, which fundamentally resolves the inherent control contradictions in the most widely-used damping control method based on frequency deviation feedback. Therefore, PFD-based VSG (PFD-VSG) exhibits the following advantages.

First, concerning the grid-connected operation mode, a) the PFD-VSG can resolve the contradiction between the response speed and the overshoot suppression ability of the active power, thereby being able to accelerate the active power response and restrain from the overshoots; b) PFD-VSG can eliminate the interactions between the droop control and the damping control, thereby achieving both the goals of droop control and damping control; c) PFD-VSG can settle the conflict between the objectives of the active power and frequency control, and thereby can obtain desirable active power and output frequency responses simultaneously.

Second, concerning the islanding operation mode, a) the PFD-VSGs can achieve an accurate load sharing in strict accordance with the power rating ratio, independent of the negative impacts of the damping control; b) PFD-VSGs can resolve the contradiction between the response speed and the overshoot suppression ability of the active power when the parameters are well-matched among the units, which is similar to the grid-connected mode; c) PFD-VSGs avoid the excessively flat ω-P characteristics, thereby preventing a small error in the control system from turning into an extremely large error of the output active power; d) PFD-VSGs have gentler transient processes of frequencies without any overshoots.

Both the theoretical analysis and the experimental results demonstrate convincingly the above conclusions. As a whole,

PFD-VSGs display better active power and frequency dynamic performance than traditional VSGs in both grid-connected and islanding operation modes.

REFERENCES

[1] Q. C. Zhong, "Power-electronics-enabled autonomous power systems: Architecture and technical routes," *IEEE Trans. Ind. Electron.*, vol. 64, no. 7, pp. 5907-5918, Jul. 2017.

[2] B. Kroposki, B. Johnson, Y. C. Zhang, V. Gevorgian, P. Denholm, B. Hodge, B. Hannegan, "Achieving a 100% renewable grid: Operating electric power systems with extremely high levels of variable renewable energy," *IEEE Power Energy Mag.*, vol. 15, no. 2, pp. 61-73, Apr. 2017.

[3] J. M. Carrasco, L. G. Franquelo, J. T. Bialasiewicz, E. Galván, R. C. Portillo Guisado, M. M. Prats, J. I. Leon, and N. Moreno-Alfonso, "Power-electronic systems for the grid integration of renewable energy sources: A survey," *IEEE Trans. Ind. Electron.*, vol. 53, no. 4, pp. 1002-1016, Aug. 2006.

[4] H. Alatrash, A. Mensah, E. Mark, G. Haddad, and J. Enslin, "Generator emulation controls for photovoltaic inverters," *IEEE Trans. Smart Grid*, vol. 3, no. 2, pp. 996-1011, Jun. 2012.

[5] M. Li, Y. Wang, W. Hu, S. Shu, P. Yu, Z. Zhang, and F. Blaabjerg, "Unified modeling and analysis of dynamic power coupling for grid-forming converters," *IEEE Trans. Power Electron*., vol. 37, no. 2, pp. 2321-2337, Feb. 2022.

[6] Q. Zhong and G. Weiss, "Synchronverters: Inverters that mimic synchronous generators," *IEEE Trans. Ind. Electron.*, vol. 58, no. 4, pp. 1259-1267, Apr. 2011.

[7] T. Shintai, Y. Miura, and T. Ise, "Oscillation damping of a distributed generator using a virtual synchronous generator," *IEEE Trans. Power Del.*, vol. 29, no. 2, pp. 668-676, Apr. 2014.

[8] S. D'Arco and J. A. Suul, "Equivalence of virtual synchronous machines and frequency-droops for converter-based microgrids," *IEEE Trans. Smart Grid*, vol. 5, no. 1, pp. 394-395, Jan. 2014.

[9] M. Li, Y. Wang, N. Xu, Y. Liu, W. Wang, H. Wang, and W. Lei, "A novel virtual synchronous generator control strategy based on improved swing equation emulating and power decoupling method," in *Proc. IEEE Energy Convers. Congr. Expo.*, Milwaukee, WI, USA, 2016, pp. 1-7.

[10] D. Dong, B. Wen, D. Boroyevich, P. Mattavelli, and Y. Xue, "Analysis of phase-locked loop low-frequency stability in three-phase grid-connected power converters considering impedance interactions," *IEEE Trans. Ind. Electron.*, vol. 62, no. 1, pp. 310-321, Jan. 2015.

[11] H. Wu *et al*., "Small-signal modeling and parameters design for virtual synchronous generators," *IEEE Trans. Ind. Electron.*, vol. 63, no. 7, pp. 4292-4303, Jul. 2016.

[12] Jia Liu, Yushi Miura, Hassan Bevrani, and Toshifumi Ise, "A unified modeling method of virtual synchronous generator for multi-operation-mode analyses," *IEEE J. Emerg. Sel. Topics Power Electron.*, vol. 9, no. 2, pp. 2394–2409, Apr. 2021.

[13] J. Alipoor, Y. Miura, and T. Ise, "Power system stabilization using virtual synchronous generator with alternating moment of inertia," *IEEE J. Emerg. Sel. Topics Power Electron.*, vol. 3, no. 2, pp. 451-458, Jun. 2015.

[14] X. Hou, Y. Sun, X. Zhang, J. Lu, P. Wang, and J. M. Guerrero, "Improvement of frequency regulation in VSG-based AC microgrid via adaptive virtual inertia," *IEEE Trans. Power Electron.*, vol. 35, no. 2, pp. 1589-1602, Feb. 2020.

[15] M. Li, Y. Wang, N. Xu, W. Wang, and J. Li, "A consistent dynamic response control strategy for virtual synchronous generator," in *IEEE 3rd Int. Future Energy Electron. Conf.*, Kaohsiung, Taiwan, China, 2017, pp. 1570-1574.

[16] F. Wang, L. Zhang, X. Feng, and H. Guo, "An adaptive control strategy for virtual synchronous generator," *IEEE Trans. Ind. Appl.*, vol. 54, no. 5, pp. 5124-5133, Sep./Oct. 2018.

[17] D. Li, Q. Zhu, S. Lin, and X. Y. Bian, "A self-adaptive inertia and damping combination control of VSG to support frequency stability," *IEEE Trans. Energy Conv.*, vol. 32, no. 1, pp. 397-398, Mar. 2017.

[18] U. Markovic, Z. Chu, P. Aristidou, and G. Hug, "LQR-based adaptive virtual synchronous machine for power systems with high inverter penetration," *IEEE Trans. Sustain. Energy*, vol. 10, no. 3, pp. 1501-1512, Jul. 2019.

[19] M. A. Torres L., L. A. C. Lopes, L. A. Morán T. and J. R. Espinoza C., "Self-tuning virtual synchronous machine: A control strategy for energy storage systems to support dynamic frequency control," *IEEE Trans. Energy Conv.*, vol. 29, no. 4, pp. 833-840, Dec. 2014.

[20] S. Qu and Z. Wang, "Cooperative control strategy of virtual synchronous generator based on optimal damping ratio," *IEEE Access*, vol. 9, pp. 709-719, Jan. 2021.

[21] X. Meng, J. Liu, and Z. Liu, "A generalized droop control for grid-supporting inverter based on comparison between traditional droop control and virtual synchronous generator control," *IEEE Trans. Power Electron.*, vol. 34, no. 6, pp. 5416-5438, Jun. 2019.

[22] X. Xiong, C. Wu, P. Cheng, and F. Blaabjerg, "An optimal damping design of virtual synchronous generators for transient stability enhancement," *IEEE Trans. Power Electron.*, vol. 36, no. 10, pp. 11026-11030, Oct. 2021.

[23] S. Dong and Y. C. Chen, "Adjusting synchronverter dynamic response speed via damping correction loop," *IEEE Trans. Energy Convers.*, vol. 32, no. 2, pp. 608-619, Jun. 2017.

[24] S. Dong and Y. C. Chen, "A method to directly compute synchronverter parameters for desired dynamic response," *IEEE Trans. Energy Convers.*, vol. 33, no. 2, pp. 814-825, Jun. 2018.

[25] M. Chen, D. Zhou, and F. Blaabjerg, "Active power oscillation damping based on acceleration control in paralleled virtual synchronous generators system," *IEEE Trans. Power Electron.*, vol. 36, no. 8, pp. 9501-9510, Aug. 2021.

[26] L. Huang, H. Xin, H. Yuan, G. Wang, and P. Ju, "Damping effect of virtual synchronous machines provided by a dynamical virtual impedance," *IEEE Trans. Energy Convers.*, vol. 36, no. 1, pp. 570-573, Mar. 2021.

[27] Y. Hirase, K. Abe, K. Sugimoto, and Y. Shindo, "A grid-connected inverter with virtual synchronous generator model of algebraic type," *Electr. Eng. Jpn.*, vol. 184, no. 4, pp. 10-21, 2013.

[28] M. Pourmohammad, M. Toulabi, and A. M. Ranjbar, "Application of state feedback controller to ensure robust D-stable operation of virtual synchronous generators," *IEEE Trans. Energy Convers.*, vol. 36, no. 2, pp. 602-610, Jun. 2021.

[29] J. Liu, Y. Miura, and T. Ise, "Fixed-parameter damping methods of virtual synchronous generator control using state feedback," *IEEE Access*, vol. 7, pp. 99177-99190, Aug. 2019.

[30] A. Karimi *et al.*, "Inertia response improvement in AC microgrids: A fuzzy-based virtual synchronous generator control," *IEEE Trans. Power Electron.*, vol. 35, no. 4, pp. 4321-4331, Apr. 2020.

[31] K. Mentesidi, R. Garde, M. Aguado, and E. Rikos, "Implementation of a fuzzy logic controller for virtual inertia emulation," in *Proc. Int. Symp. Smart Electr. Distrib. Syst. Technol.*, 2015, pp. 606-611.

[32] Q. Xu, T. Dragicevic, L. Xie, and F. Blaabjerg, "Artificial intelligence-based control design for reliable virtual synchronous generators," *IEEE Trans. Power Electron.*, vol. 36, no. 8, pp. 9453-9464, Aug. 2021.

[33] A. S. Mir and N. Senroy, "Self-tuning neural predictive control scheme for ultrabattery to emulate a virtual synchronous machine in autonomous power systems," *IEEE Trans. Neural Netw. Learn. Syst.*, vol. 31, no. 1, pp. 136-147, Jan. 2020.

[34] F. Yao, J. Zhao, X. Li, L. Mao, and K. Qu, "RBF neural network based virtual synchronous generator control with improved frequency stability," *IEEE Trans. Ind. Inform.*, vol. 17, no. 6, pp. 4014-4024, Jun. 2021.

[35] S. D'Arco, J. A. Suul, and O. B. Fosso, "A virtual synchronous machine implementation for distributed control of power converters in SmartGrids," *Electr. Power Syst. Res.*, vol. 122, pp. 180-197, 2015.

[36] Y. Hirase, K. Sugimoto, K. Sakimoto, and T. Ise, "Analysis of resonance in microgrids and effects of system frequency stabilization using a virtual synchronous generator," *IEEE J. Emerg. Sel. Topics Power Electron.*, vol. 4, no. 4, pp. 1287-1298, Dec. 2016.

Mingxuan Li (Member, IEEE) received the Ph.D. degree in electrical engineering from Xi'an Jiaotong University, Xi'an, China, in 2020. From 2017 to 2019, he was a visiting scholar with the Department of Energy Technology, Aalborg University, Aalborg, Denmark.

He is currently a Postdoctoral Researcher in control science and engineering with University of Electronic Science and Technology of China (UESTC). His research interests include distributed power generation systems, microgrids, stability analysis and control of converter-based systems, and artificial intelligence in modern power systems.

Peng Yu received the B.S. degree in electrical engineering from Guangxi University, Nanning, China, in 2017. He is currently pursuing the M.S. degree in electrical engineering in Xi'an Jiaotong University.

His research interests include the modeling and control of converters, and renewable energy integration.

Weihao Hu (Senior Member, IEEE) received the B.Eng. and M.Sc. degrees from Xi'an Jiaotong University, Xi'an, China, in 2004 and 2007, respectively, both in electrical engineering, and Ph. D. degree from Aalborg University, Denmark, in 2012.

He is currently a Full Professor and the Director of Institute of Smart Power and Energy Systems (ISPES) at the University of Electronics Science and Technology of China (UESTC). He was an Associate Professor at the Department of Energy Technology, Aalborg University, Denmark and the Vice Program Leader of Wind Power System Research Program at the same department. His research interests include artificial intelligence in modern power systems and renewable power generation. He has led/participated in more than 15 national and international research projects and he has more than 170 publications in his technical field.

He is an Associate Editor for IET Renewable Power Generation, a Guest Editor-in-Chief for Journal of Modern Power Systems and Clean Energy Special Issue on Applications of Artificial Intelligence in Modern Power Systems, a Guest Editor-in-Chief for Transactions of China Electrical Technology Special Issue on Planning and operation of multiple renewable energy complementary power generation systems, and a Guest Editor for the IEEE TRANSACTIONS ON POWER SYSTEMS Special Section on Enabling very high penetration renewable energy integration into future power systems. He was serving as the Technical Program Chair (TPC) for IEEE Innovative Smart Grid Technologies (ISGT) Asia 2019 and is serving as the Conference Chair for the Asia Energy and Electrical Engineering Symposium (AEEES 2020). He is currently serving as Chair for IEEE Chengdu Section PELS Chapter. He is a Fellow of the Institution of Engineering and Technology, London, U.K. and an IEEE Senior Member.

Yue Wang (Member, IEEE) was born in Liaoning, China, in 1972. He received the B.S. degree from Xi'an Jiaotong University, Xi'an, China, in 1994, the M.S. degree from Beijing Jiaotong University, Beijing, China, in 2000, and the Ph.D. degree from Xi'an Jiaotong University in 2003, all in electrical engineering.

He is currently a Full Professor with the School of Electrical Engineering, Xi'an Jiaotong University. His research interests include wireless power transfer, active power filters, multilevel converters, and HVDC.

Sirui Shu received the B.S. degree in electrical engineering from Xi'an Jiaotong University, Xi'an, China, in 2019, where she is currently pursuing the M.S. degree in electrical engineering.

Her research interests include the modeling and control of converters, and renewable energy integration.

Zhenyuan Zhang (Senior Member, IEEE) received the B.S. degree from Chang'an University, Xi'an, China, in 2007, and the Ph.D. degree from the University of Texas at Arlington, Arlington, TX, USA, in 2015, all in Electrical Engineering.

He is currently a Professor with the School of Mechanical and Electrical Engineering, University of Electronic Science and Technology of China, Chengdu, China. Since 2010, he has been the Project Associate with the IEEE/NFPA Arc Flash Research Project. His focus lies in smart grids and arc flash research, but he has also been involved in power system analysis, renewable energy, electrical safety analysis, and power market researches.

Frede Blaabjerg (Fellow, IEEE) was with ABB-Scandia, Randers, Denmark, from 1987 to 1988. From 1988 to 1992, he got the PhD degree in Electrical Engineering at Aalborg University in 1995. He became an Assistant Professor in 1992, an Associate Professor in 1996, and a Full Professor of power electronics and drives in 1998. From 2017 he became a Villum Investigator. He is honoris causa at University Politehnica Timisoara (UPT), Romania and Tallinn Technical University (TTU) in Estonia.

His current research interests include power electronics and its applications such as in wind turbines, PV systems, reliability, harmonics and adjustable speed drives. He has published more than 600 journal papers in the fields of power electronics and its applications. He is the co-author of four monographs and editor of ten books in power electronics and its applications.

He has received 32 IEEE Prize Paper Awards, the IEEE PELS Distinguished Service Award in 2009, the EPE-PEMC Council Award in 2010, the IEEE William E. Newell Power Electronics Award 2014, the Villum Kann Rasmussen Research Award 2014, the Global Energy Prize in 2019 and the 2020 IEEE Edison Medal. He was the Editor-in-Chief of the IEEE TRANSACTIONS ON POWER ELECTRONICS from 2006 to 2012. He has been Distinguished Lecturer for the IEEE Power Electronics Society from 2005 to 2007 and for the IEEE Industry Applications Society from 2010 to 2011 as well as 2017 to 2018. In 2019-2020 he serves as President of IEEE Power Electronics Society. He is Vice-President of the Danish Academy of Technical Sciences too. He is nominated in 2014-2019 by Thomson Reuters to be between the most 250 cited researchers in Engineering in the world.